Journal of Geophysical Research: Solid Earth

RESEARCH ARTICLE
10.1029/2018JB015985

On the Mechanical Effects of Poroelastic Crystal Mush in Classical Magma Chamber Models

Yang Liao[1], **S. Adam Soule**[1], **and Meghan Jones**[1]

[1]Department of Geology and Geophysics, Woods Hole Oceanographic Institution, Woods Hole, MA, USA

Key Points:
- A new model provides the first constraints on the mechanical effects of poroelastic mush in a magma chamber
- Crystal much results in a transient evolution of core pressure and tensile stresses at the chamber margins during and after an injection
- Poroelasticity, in contrast to viscoelasticity, results in a postinjection evolution time scale that is dependent on the magma chamber size

Correspondence to:
Y. Liao,
yliao@whoi.edu

Citation:
Liao, Y., Soule, S. A., & Jones, M. (2018). On the mechanical effects of poroelastic crystal mush in classical magma chamber models. *Journal of Geophysical Research: Solid Earth*, *123*, 9376–9406. https://doi.org/10.1029/2018JB015985

Received 19 APR 2018
Accepted 23 SEP 2018
Accepted article online 30 SEP 2018
Published online 8 NOV 2018

Abstract Improved constraints on the mechanical behavior of magma chambers is essential for understanding volcanic processes; however, the role of crystal mush on the mechanical evolution of magma chambers has not yet been systematically studied. Existing magma chamber models typically consider magma chambers to be isolated melt bodies surrounded by elastic crust. In this study, we develop a physical model to account for the presence and properties of crystal mush in magma chambers and investigate its impact on the mechanical processes during and after injection of new magma. Our model assumes the magma chamber to be a spherical body consisting of a liquid core of fluid magma within a shell of crystal mush that behaves primarily as a poroelastic material. We investigate the characteristics of time-dependent evolution in the magma chamber, both during and after the injection, and find that quantities such as overpressure and tensile stress continue to evolve after the injection has stopped, a feature that is absent in elastic (mushless) models. The time scales relevant to the postinjection evolution vary from hours to thousands of years, depending on the micromechanical properties of the mush, the viscosity of magma, and chamber size. We compare our poroelastic results to the behavior of a magma chamber with an effectively viscoelastic shell and find that only the poroelastic model displays a time scale dependence on the size of the chamber for any fixed mush volume fraction. This study demonstrates that crystal mush can significantly influence the mechanical behaviors of crustal magmatic reservoirs.

1. Introduction

Crustal magmatic reservoirs play a crucial role in the storage and transport of magma and gas that erupt on Earth's surface, and their properties can strongly influence the triggering, duration, and style of volcanic eruptions. Although the processes in magma chambers cannot be directly observed, advancements in high-precision monitoring via satellite imaging, seismic measurements, gas composition and flux, and tilt meters allow us to detect mechanical processes happening in the plumbing system, such as magma injection or withdrawal, chamber pressurization and expansion, and magma transport. For example, measurements of ground deformation caused by injection of magma into a chamber have frequently been used to infer magma recharge and predict future unrest (Browning et al., 2015; Davis, 1986; Dzurisin, 2003; Le Mével et al., 2016; Lu & Dzurisin, 2010; Masterlark, 2007; Srigutomo et al., 2015; Voight et al., 2006; Wicks et al., 2002). Ground deformation data are conventionally analyzed and interpreted using mechanical models of magma chambers, leading to an approximation of the amount of injected magma. The mechanical models invoked in analyzing crustal deformation data typically center around the concept of a crustal magma chamber consisting of liquid magma within the elastic crust. The principles of continuum physics are invoked to quantitatively link the deformation of crust and magma chamber with events such as magma injection, surface pressure unloading, and gas exsolution (Chouet et al., 2006; McTigue, 1987; Mogi, 1958; Nishimura, 2006; Rivalta, 2010). Based on the same concept, more realistic considerations for sill-shaped magma chambers, as well as viscoelastic rheology of the high-temperature crustal rocks, have also been implemented (Amoruso & Crescentini, 2009; Dragoni & Magnanensi, 1989; Karlstrom et al., 2010; Segall, 2016).

Although most mechanical models for volcano/ground deformation assume fluid magma chambers residing in solid rocks to be the center of the crustal igneous processes, petrological studies and observations from fossil magma chambers have long pointed to the existence of crystal mush in the crustal plumbing system (e.g., Gudmundsson, 1987; Hildreth & Lanphere, 1994; Marsh, 1989). The concept of a *mushy* crustal plumbing system, wherein crystalline mush can occupy more than 70% of the magmatic reservoir and prevent direct mechanical connection between the liquid magma and the crustal rock, has been increasingly explored

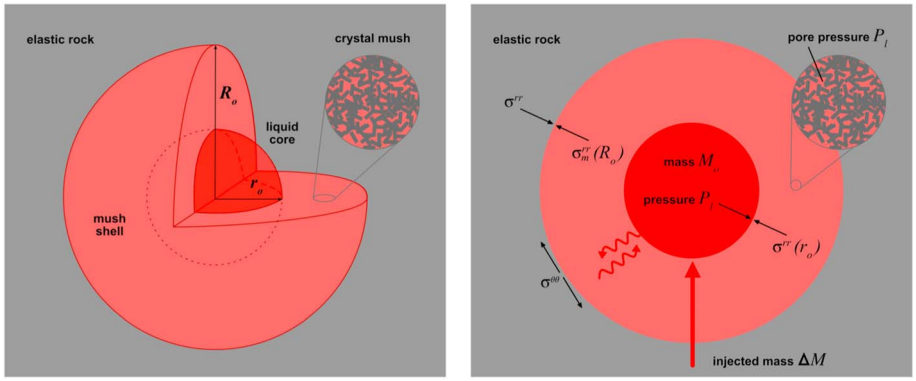

Figure 1. Three-dimensional (left) and plane (right) view of the geometry of the model. The spherical magma chamber has radius R_o, which consists of a liquid core with radius r_o and a crystal mush shell with thickness $R_o - r_o$ and porosity ϕ_o. The chamber is surrounded by an infinite domain of elastic host rock. The mush, shown in circular insets, consists of solid crystals and pore fluid magma. The boundary conditions, including force balances at the inner and outer boundaries of the mush shell, are shown by black arrows.

and emphasized in recent studies (e.g., Bachmann & Huber, 2016; Barboni et al., 2016; Cashman et al., 2017; Gelman et al., 2013; Karakas et al., 2017; Singer et al., 2018; Sparks & Cashman, 2017; Szymanowski et al., 2017). These studies have suggested that abundant crystal mush strongly impacts the thermal and chemical evolution in magmatic systems through processes of melt infiltration and segregation and may limit or enhance the eruptability of a magmatic system (Anderson et al., 1984; Bachmann & Bergantz, 2004, 2006; Bergantz et al., 2006, 2015; Degruyter & Huber, 2006, 2014; Huber et al., 2010, 2011; Mourtada-Bonnefoi et al., 1999, 2011; Parmigiani et al., 1999, 2014; Sisson & Bacon, 1999). These studies largely deal with internal dynamics of a mushy magma chamber, but fewer studies have examined chamber- to crustal-scale mechanical processes. Some notable exceptions include studies on a completely mushy, poroelastic magma chamber, which demonstrated that magma can be erupted despite the absence of a fully liquid region (Gudmundsson, 2012, 2016).

The mechanical processes reflected in evolving chamber pressures and crustal deformation for magma chambers containing both liquid and mush regions are less well defined, but are likely relevant for natural magmatic systems in which the crystallization front propagates inward (Marsh, 1989). Abundant two-phase, magma-crystal ensembles surrounding the liquid portion of magma chambers may modify the deformation and stresses in the crust. To understand how the plumbing system behaves mechanically in the presence of crystal mush, the conventional *mushless* models need to be reexamined and modified. Here we report on a new analytical model that we use to interrogate the influence of crystal mush on the mechanical processes during and after magma injection into an existing chamber. Specifically, we consider the effect of the poroelasticity of the mush on the changes in mechanical states of the chamber and the crustal rocks, such as chamber pressure and tensile stress. Our model provides a novel framework that incorporates three components, liquid compressible magma, permeable poroelastic mush, and elastic crustal rocks and enables us to quantitatively examine the effects of crystal mush during magma injection events.

2. Mushy Magma Chamber Models

2.1. Poroelasticity of the Crystal Mush

Crystal mush forms when the volume fraction of crystals in a crystal-magma suspension is large enough such that the suspension becomes rheologically locked (e.g., Marsh, 1989). As the magma cools and the volume fraction of crystals increases, two transitions occur that make the magma-crystal ensemble display features of a solid: First, the effective viscosity of the suspension increases sharply at a crystallinity of ~40% (the specific volume fraction varies with crystal shape and size distribution), reducing the ability of the suspension to flow as a fluid (Caricchi & Blundy, 2015; Costa, 2005; Costa et al., 2009; Lejeune & Richet, 1995; Moitra & Gonnermann, 2015; Picard et al., 2011; Pistone et al., 2012; Vigneresse et al., 1996). Second, as the volume fraction increases to a critical value, the crystals form a touching network, which behaves as a solid, elastic frame that resists deformation (Aharonov & Sparks, 1999; Jerram et al., 2003). Some studies have suggested a poroelastic rheology for partially molten magma chambers (Gudmundsson, 1987, 2012; Nooner & Chadwick, 2009). Specifically, Nooner and Chadwick (2009) suggested that poroelasticity, in addition to viscoelastic relaxation

of the crust, could explain the field observation of posteruption repressurization of a mid-ocean ridge volcano. In this study, we consider crystal mush to behave poroelastically. We compare this to another case where the crystalline framework deforms viscoelastically.

2.2. Model Setup

We develop a conceptual model for a mushy magma chamber that is subjected to a magma injection event in order to interrogate the mechanical effects of crystal mush in the chamber. Our model assumes a simplified, radially symmetric (i.e., spherical) magma chamber for convenience of analysis and to facilitate comparisons with existing models (e.g., Dragoni & Magnanensi, 1989; Karlstrom et al., 2010; McTigue, 1987). In the magma chamber, a liquid core of compressible magma is surrounded by a spherical shell of poroelastic crystal mush with porosity ϕ_o. All pore spaces in the mush are filled with magma. The magma chamber sits within an infinite domain of homogeneous, isotropic host rock, which is assumed to be a linear elastic material (Figure 1). Prior to the injection of new magma, the magma chamber is in lithostatic equilibrium, where the stresses in the mush shell and host rock, as well as the core fluid pressure, balance at both the fluid-mush interface and the mush-rock interface. For simplicity, we consider the materials to be isotropic and homogenous; thus, material failures (fracture formation, diking, etc.) are not considered.

A simplified magma injection event begins at time $t = 0$, after which a specific amount of magma is added into the fluid core over a finite time interval. We assume that the volume of the injected magma is small compared to that of the liquid core, thus leading to reversible deformation in the mush shell and host rocks. By invoking principles of linear elasticity and poroelasticity, we examine the change in deformation and stresses in the system from the initial steady state. For consistency with existing mushless mechanical models, we consider the processes involved during and after the injection to be isothermal (Browning et al., 2015; Mogi, 1958; Segall, 2016); thus, the rheologies of the material remain constant.

During and after the injection, the displacement increments are denoted by $\vec{u}_{\text{rock}}$ in the host rock and $\vec{u}_m$ in the mush shell. Assuming spherical symmetry, the displacements only contain radial components; hence, $\vec{u}_{\text{rock}} = u_{\text{rock}}(r,t)\hat{r}$ and $\vec{u}_m = u_m(r,t)\hat{r}$, where $\hat{r}$ is the radial basis in the spherical coordinate, pointing outward; r is the radial position, measured from the center of the chamber to the initial position of any given point in the mush shell or host rock; and t is time, measured from the onset of the magma injection. The change in elastic or poroelastic stresses from deformations is $\boldsymbol{\sigma}_{\text{rock}}(r,t)$ in the host rock and $\boldsymbol{\sigma}_m(r,t)$ in the mush shell. Due to radial symmetry, the stress tensors only have nonzero values in the radial components $\sigma^{rr}_{\text{rock}}(r,t)$, $\sigma^{rr}_m(r,t)$, and tensile components $\sigma^{\theta\theta}_{\text{rock}} = \sigma^{\phi\phi}_{\text{rock}}$, $\sigma^{\theta\theta}_m = \sigma^{\phi\phi}_m$. The injection event is modeled by an increase in the core fluid mass, which starts at time $t = 0$. We assume that during the injection, magma is added to the chamber at a constant rate. That is, for the same injected mass, a longer injection period corresponds to the smaller injection rate; when the injection rate is infinitely high, we refer to the case as a sudden injection. For convenience, we refer to the case of spherical magma chamber with no mush as the *elastic* model.

2.3. Governing Equations and Quantitative Solutions

2.3.1. Deformation and Fluid Transport in the Mush Shell

We consider the crystal mush to be an ideal (i.e., homogeneous and isotropic) poroelastic material and apply the classical theories for linear poroelasticity developed by Biot (1941) to describe its deformation. We define the variation in fluid content $m(r,t)$ as the change in pore fluid mass per undeformed volume of the mush, which has unit of density. By this definition, $m > 0$ indicates that pore fluid is gained, and $m < 0$ indicates that pore fluid is lost relative to the initial condition. The constitutive relations for an ideal poroelastic material prescribe the linear relations between the strain (i.e, determined by $\vec{u}_m(r,t)$), stress $\boldsymbol{\sigma}_m(r,t)$, pore pressure $P_f(r,t)$, and variation in fluid content $m(r,t)$

$$\boldsymbol{\sigma}_m = (K_m - \frac{2}{3}\mu_m)\nabla\cdot\vec{u}_m(r)\boldsymbol{I} + \mu_m\left(\nabla\vec{u}_m + \nabla\vec{u}_m^T\right) - \alpha P_f\boldsymbol{I} \tag{1a}$$

$$m = \rho_f\alpha(\nabla\cdot\vec{u}_m + \frac{\alpha}{K_u - K_m}P_f), \tag{1b}$$

where $\boldsymbol{I}$ is the unit tensor. The constitutive relations include several micromechanical properties of the mush (see Table A2 for their definitions). For example, the undrained modulus K_u and the drained modulus K_m indicate the strength of mush for a given volumetric deformation with and without the participation of pore fluid. Specifically, K_u depends on the strength of the solid crystals, strength of the pore structure, and the compressibility of the pore fluids, while K_m depends only on the strength of the solid crystals and the strength of the pore structure in the mush.

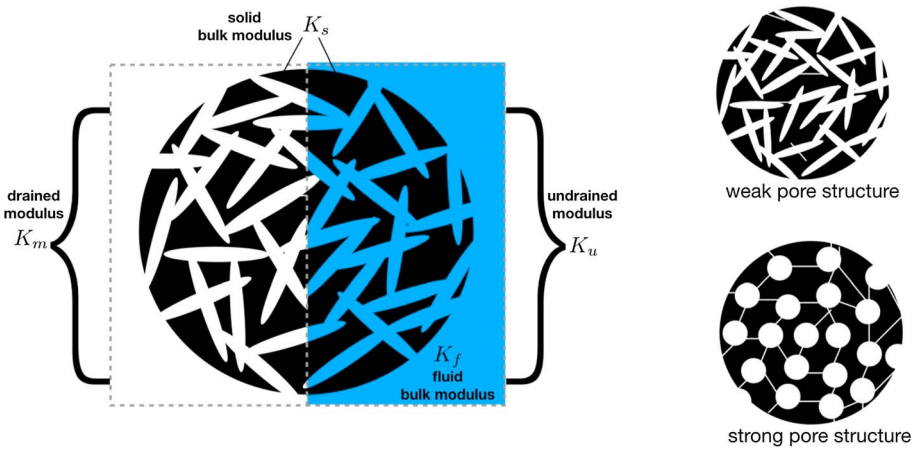

Figure 2. (left panel) The relations between the bulk moduli of the porous ensemble K_m, K_u, and the bulk moduli of the separate phases. K_m is the drained bulk modulus, which is determined by the bulk modulus for the solid phase K_s, and the structural strength of the pore space. K_u is the undrained bulk modulus, which is determined by K_s, the structural strength of pore space, and the bulk modulus (inverse of compressibility) K_f of the fluid phase. (right panel) Two cases with different structural strengths of the pore space: the structure consisting spherical pores are stronger, while slit-like pores are weaker (Cheng, 2016).

A unique property of poroelastic material, compared to elastic material, is that the pore fluids accommodate a portion of the applied stress on the ensemble, which is reflected by the coefficient α in the last term on the right-hand side of (1a). The poroelastic coefficient α (also known as Biot coefficient) can be further estimated via

$$\alpha = 1 - \frac{K_m}{K_s}, \tag{2}$$

where K_s is the bulk modulus of the crystals in the mush. Typically, the bulk modulus K_m of the dry solid with interstitial spaces is smaller than K_s, leading to the range of α between 0 to 1. For the crystal mush, we assume that the fluid magma is distributed along the boundaries of the crystals and hence forms pore spaces that are closer to slit shaped, rather than sphere shaped. Slit-shaped pore spaces in the crystal mush tend to weaken the pore structure (see Figure 2), lowering the value of K_m and increasing the coefficient α. We consider a large value of α (i.e., 0.5 – 1) to be more likely for the crystal mush.

We assume the mush shell to be permeable and that the fluid occupying the interstitial spaces flows according to Darcy's law in which $\vec{q}$ is the Darcy velocity of the pore fluid, κ is the permeability of the porous crystalline structure in the mush, η_f is the viscosity of the pore fluid magma, and ρ_f is the density of the pore fluid magma:

$$\vec{q} = -\frac{\kappa}{\eta_f}\nabla P_f \tag{3a}$$

$$\frac{\partial m}{\partial t} + \nabla \cdot (\rho_f \vec{q}) = 0 \tag{3b}$$

in which (3b) is the mass conservation of the pore fluid mass and (3a) is the Darcy's law for porous flow (we assume negligible gravitational force relative to pressure gradient).

2.3.2. Deformation in Crust Rock and Core Fluid Pressure

The deformation in the crustal rock caused by the inflation of the magma chamber and the generated stress are linked by the constitutive relation for a linear elastic solid:

$$\boldsymbol{\sigma}_{\text{rock}} = (K_r - \frac{2}{3}\mu_r)\nabla \cdot \vec{u}_{\text{rock}}\boldsymbol{I} + \mu_r\left(\nabla\vec{u}_{\text{rock}} + \nabla\vec{u}_{\text{rock}}^{T}\right), \tag{4}$$

where K_r and μ_r are the bulk and shear modulus of the host rock, respectively.

Magma chamber inflation results from injecting magma of finite mass ΔM into a chamber with a liquid core of mass M_o. At any moment t, we define $M_{\text{inj}}(t)$ as the amount of magma that has been injected into the liquid core between time 0 to t. As magma can be driven across the liquid-mush interface, we define $M_{\text{leak}}(t)$ as the total mass of magma that has been transported into the mush shell at any given time, which is related

to the variable $m(r,t)$, defined as the variation of fluid content in (1b) as $M_{\text{leak}}(t) = \int_{r_o}^{R_o} 4\pi r^2 m(r,t)\mathrm{d}r$, due to the conservation of fluid mass. We assume that isothermal compression of the core fluid during and after the injection causes the core pressure to increase and find that the increase in core pressure $P_l(t)$ is

$$P_l(t) = K_l\left(\frac{M_{\text{inj}}(t)}{M_o} - \frac{M_{\text{leak}}(t)}{M_o}\right)\left(1 - 3\frac{u_m(r_o,t)}{r_o}\right), \tag{5}$$

where K_l is the bulk modulus (i.e., inverse of compressibility) of the core magma and $u_m(r_o,t)$ indicates the radial displacement at the boundary $r = r_o$ on the liquid-mush interface (derived in Appendix A1). In our study, we explore two types of injection: gradual injection where the injected magma ΔM is added into the chamber with a constant mass flow rate over a period from $t = 0$ to $t = t_{\text{inj}}$ and sudden injection where the same amount of magma is added into the liquid core instantaneously at time 0. The two cases lead to the expression for $M_{\text{inj}}(t)$:

$$M_{\text{inj}}(t) = \begin{cases} \frac{\Delta M}{t_{\text{inj}}}\left(t - (t - t_{\text{inj}})H(t - t_{\text{inj}})\right), \text{for gradual injection} \\ \Delta M \qquad\qquad\qquad\quad \text{, for sudden injection} \end{cases}, \tag{6}$$

where H is the Heaviside function.

2.3.3. Boundary Conditions

We assume that the elastic host rock and elastic solid network in the mush are at quasi-equilibrium state due to the rapidity of the elastic response of the solid matrix; hence,

$$\nabla \cdot \sigma_{\text{rock}}(r,t) = 0, \qquad \nabla \cdot \sigma_m(r,t) = 0. \tag{7}$$

The combination of equations (7), ((1)), and (3) leads to a diffusion equation for $m(r,t)$ (see Appendix A2.3):

$$\frac{\partial}{\partial t}m - c\nabla^2 m = 0 \tag{8}$$

where the poroelastic diffusivity c is defined as

$$c = \frac{\kappa}{\eta}\frac{(K_m + \frac{4}{3}\mu_m)(K_u - K_m)}{\alpha^2(K_u + \frac{4}{3}\mu_m)}, \tag{9}$$

which is controlled by the micromechanical properties of the mush (e.g., K_m, K_u, and μ_m). The solution for (8), which will lead to the solution of other quantities in the system, is determined by the boundary conditions. Forces are mechanically balanced on both the liquid-mush interface and the mush-rock interface, leading to

$$P_l(t) + \sigma_m(r_o,t) = 0 \tag{10a}$$

$$\sigma_m^{rr}(R_o,t) = \sigma_{\text{rock}}^{rr}(R_o,t) \tag{10b}$$

$$\vec{u}_m(R_o,t) = \vec{u}_{\text{rock}}(R_o,t), \tag{10c}$$

where (10c) requires the continuity of displacement across the mush-rock boundary. For the pore fluid, we assume that fluid pressure at the core-mush interface is continuous and that the mush-rock interface is impermeable for the magma:

$$P_f(r_o,t) = P_l(t) \qquad (t>0) \tag{11a}$$

$$\nabla P_f(R_o,t) = 0. \tag{11b}$$

2.3.4. Solution Method

To facilitate solving for the evolution of the system, we choose the chamber radius R_o for the length scale, the poroelastic diffusion time $\frac{R_o^2}{c}$ for the time scale, the preinjection density of magma $\rho_{f,(0)}$ for the scale of m, and the elastic rigidity of the host rock μ_r for the scale of stress or pressure. We nondimensionalize the variables in the governing equations and boundary conditions using their respective scales and obtain a governing equation for the dimensionless variation in fluid content m (for convenience, we use the same symbols for the dimensionless variables):

$$\frac{\partial}{\partial t}m(r,t) - \nabla^2 m(r,t) = 0. \tag{12}$$

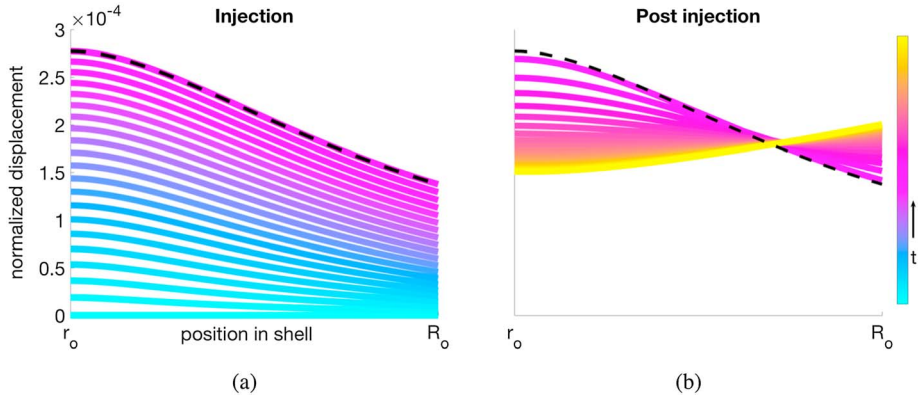

Figure 3. Deformation in the mush shell (a) during and (b) after an injection. The radial displacement in the mush shell is shown as function of radial position in the mush shell. The color indicates a progression in time during and after the injection: The injection period is shown from blue to magenta, and the postinjection evolution is shown from magenta to yellow. During the injection, all points in the mush shell push radially outward; after the injection, the inner rim of the shell retracts inward due to the loss of fluid from the liquid core, while the outer rim continues to push outward, due to the inflation of the shell caused by increased fluid content. The maximum displacement at the core-shell boundary occurs at the end of the injection, as shown by the black dashed line. The evolution is calculated numerically using a finite difference scheme, for a system with parameter set #1 from Table A3.

The boundary conditions (10) and (11) can be transformed into constraints on m at the two boundaries (note that after being normalized by the length scale, the inner and outer boundary of the mush shell corresponds to $r = \frac{r_o}{R_o}$ and 1, respectively):

$$f_1 m\left(\frac{r_o}{R_o}, t\right) + h_0 \int_{\frac{r_o}{R_o}}^{1} m(r', t) r'^2 \mathrm{d}r' = h_1, \quad (t > 0) \tag{13a}$$

$$\frac{\partial m}{\partial r}(1, t) = 0, \quad (t > 0) \tag{13b}$$

$$m(r, 0) = 0, \quad \left(\frac{r_o}{R_o} < r < 1\right), \tag{13c}$$

where (13c) is the initial condition for m, indicating that initially the pore fluids are not moving. The constants h_0, f_1, and h_1 are determined by the micromechanical properties of the liquid-filled mush material and the geometrical property r_o/R_o of the magma chamber (see Appendices A2.5 and A2.6). We solve (12) with the boundary conditions (13) numerically and analytically for the evolution of $m(r, t)$ during and after the injection. Once $m(r, t)$ is obtained, other quantities, including the displacement, stresses, and pressures, can be determined (see Appendix A2.5). We identify how these quantities evolve with time, the new steady state reached by the system after the injection, and the time it takes for the system to arrive at the new steady state.

3. Syn-injection and Postinjection Evolution

One distinct feature of the mush model, compared to the conventional elastic model, is that the mechanical state of both the chamber itself and the host rock surrounding it can evolve after an injection has terminated. In this section, we explore the postinjection evolution of the core liquid pressure and the tensile stress in the host rock. Both of these properties are thought to play important roles in magmatic systems, as the former can modulate the injection rate, and the latter may cause wall rock to rupture and trigger an eruption (Blake, 1981; Gudmundsson, 2016; McTigue, 1987; Segall, 2016). As the injection rate of magma can vary many orders of magnitude in nature (Crisp, 1984), we select a variety of injection rates (by varying the injection time t_{inj} for the same volume of magma) in order to qualitatively understand the impact of injection rate on the transient evolution of the system. Realistically, the injection rate is likely modulated by the change in the liquid core pressure, which we discuss in section 6. For simplicity, we assume that the injection rate is a constant during the injection and instantaneously becomes 0 once the injection terminates.

3.1. Transient Evolution of Deformation and Stresses

We find that the deformation in the mushy chamber and host rock and the liquid core pressure and host rock tensile stress all increase during the injection and continue to evolve after the injection terminates. The liquid

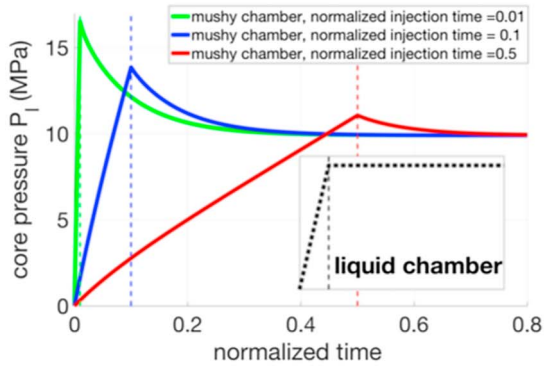

(a)

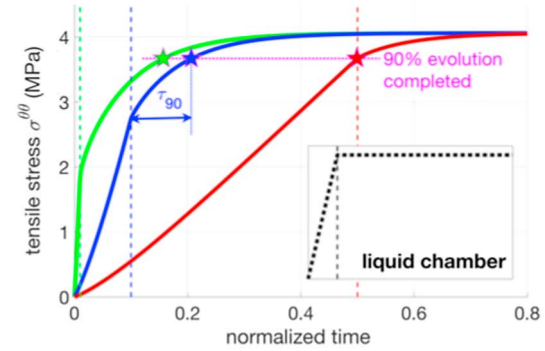

(b)

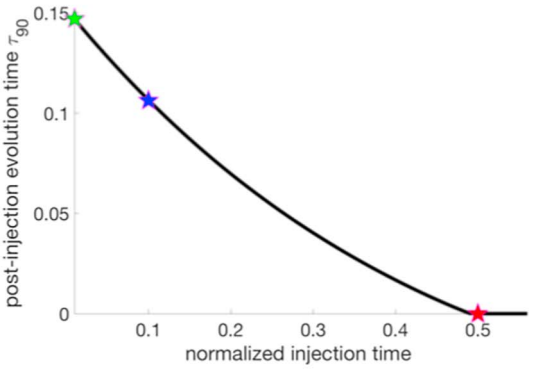

(c)

Figure 4. Evolution of (a) core pressure P_l and (b) tensile stress $\sigma^{\theta\theta}_{\text{rock}}$ in the rock at the mush-rock boundary as functions of time t (normalized), for three different injection times t_{inj} (normalized), respectively. The vertical dash lines in green, blue, and red indicate the moments when the injection terminates, at $t = 0.01$, $t = 0.1$, and $t = 0.5$, respectively. Insets in (a) and (b) show the evolutions of the core pressure and tensile stress corresponding to a liquid magma chamber model with the same liquid core volume, for which both quantities linearly increase with time and stop changing once the injection terminates (indicated by the black vertical dash line). The horizontal dash line in magenta indicates 90% of the final steady tensile stress, intersecting with the three curves, as indicated by the green, blue, and red stars. The definition for τ_{90} is shown for the case of $t_{\text{inj}} = 0.1$, indicated by the blue star and arrow. (c) The (normalized) postinjection evolution time τ_{90}, defined as the extra postinjection time before the tensile stress reaches 90% of its final steady value. Green, blue, and red stars correspond to the three different injection times shown in panel (b). For large injection time t_{inj} (e.g., when $t_{\text{inj}} \geqslant 0.5$), the system would have reached more than 90% of the final stress before the injection terminates, in which case $\tau_{90} = 0$. For all four panels, the system has parameter set #1 from Table A3.

core pressure reaches its maximum at the end of the injection period and decreases during the postinjection evolution, while the tensile stress on the host rock, in most cases, keeps increasing during the postinjection evolution. Thus, in most cases the whole magma chamber continues to inflate after the injection event (see Figures 3 and 4).

We find that the fluid content within the mush shell increases and the volume of the liquid core decreases after the injection ceases (see Appendix A2.6 and Figure A1). This reflects diffusion of magma into the poroelastic mush shell, which causes the postinjection evolution of the system. During the injection, the fluid pressure gradient across the liquid-mush boundary increases and drives the diffusion of magma content from the inner boundary of the mush shell toward the outer boundary. As the speed of this process is limited by the finite diffusivity, the pressure gradient in the mush is not eliminated at the time the injection terminates, resulting in continued melt transport and deformation during the postinjection evolution (Figure 3). Because the magma is injected into the fluid core, the pressure in the liquid core is always higher than in the mush immediately after the injection ceases. As a result, the core fluid pressure and volume always decrease due to the porous flows during the postinjection period. Meanwhile, as more magma is transported into the mush shell, the pore spaces in the mush swell and the mush shell volume increases during the postinjection evolution. In the example shown in Figure 3, the porosity in the mush shell increases by only 0.001–0.002 (see Figure A1 in Appendix A2.6), which is still well within the limits of a locked/uneruptable mush (Cashman et al., 2017). The postinjection change in the total volume of the magma chamber, hence the tensile stress in the host rock, results from the combined effects of the *shrinking* liquid core and the *swelling* mush shell and may either increase (Figure 4b) or decrease (discussed in section 4), depending primarily on the value of α. However, we find that a postinjection increase in the total chamber volume is more likely to occur, given the expected large value of α for the crystal mush ensemble (as discussed in section 2.3.1), as well as the high compressibility of the core magma compared to the host rock.

3.2. Characteristic Time for Postinjection Evolution

With enough time postinjection, the system approaches a steady state (Figure 4). In contrast, if a liquid magma chamber is mushless (as in the conventional elastic models), a new steady state is reached as soon as the injection terminates due to the instantaneous elastic deformation in the wall rock (insets in Figures 4a and 4b). In this section, we quantify the time scale associated with the postinjection poroelastic evolution, using the analytical solution for the case of a sudden injection. Following a sudden injection, the time-dependent solutions involve an infinite number of exponentially decaying terms with the form

$$A_0(r) + A_1(r)e^{-x_1 t} + A_2(r)e^{(-x_2 t)} + \ldots + A_n(r)e^{-x_n t} + \ldots,$$

where $A_0, A_1, A_2, \ldots, A_n, \ldots$ are r-dependent coefficients, and positive values $x_1 < x_2 < \ldots < x_n < \ldots$ determine the decay rate for each term. The smallest decay rate x_1, calculated graphically using Laplace transform, yields the longest and most dominant decay time (see Appendix A2.7 for details). This dominant time scale occurs when injection time $t_{\text{inj}} \to 0$ (Figure 4c), and is defined as

$$t_{\text{post}} = (R_o^2/c) * (1/x_1)$$

in which (R_o^2/c) is the poroelastic diffusion time (see Appendix A2.8). The t_{post} is determined by the geometry of the system and physical properties of the magma and mush. We find that t_{post} is strongly positively and nonlinearly influenced by the volume fraction of mush in the chamber and the poroelastic coefficient α (see Figure 5). The relationship between t_{post} and α suggests that slit-shaped interstitial spaces in crystal mush favor longer postinjection time. Other micromechanical properties, such as the relative mush rigidity $\frac{\mu_m}{\mu_r}$, the compressibility of the core magma $\frac{K_l}{\mu_r}$, and pore magma $\frac{K_f}{\mu_r}$, (see Appendix A2.8 and Table A2), also affect t_{post} nonlinearly, but to a lesser degree (see Figure A3b in Appendix A2.8).

In addition to the dimensionless parameters that influence t_{post} nonlinearly, we find that t_{post} also increases linearly with a lumped parameter $t_{\text{post}} \propto \frac{R_o^2 \eta_f}{\kappa \mu_r}$. Thus, t_{post} generally increases with larger chamber size and higher magma viscosity, and decreases with increasing mush permeability. Figure 5 illustrates that t_{post} can vary from hours to over 1,000 years using liquid core radii from 0.1 to 5 km, mush permeability κ from 10^{-10} – 10^{-8} m^2, rock rigidity μ_r of ~10 GPa, and magma viscosity from 10^2–10^6 Pa s.

4. Effects of Crystal Mush on the Postinjection Steady State

After an injection, a steady state is eventually achieved when the fluid pressure reaches a uniform value in the mush shell. The displacement and stresses in this new steady state, which correspond to their solutions at

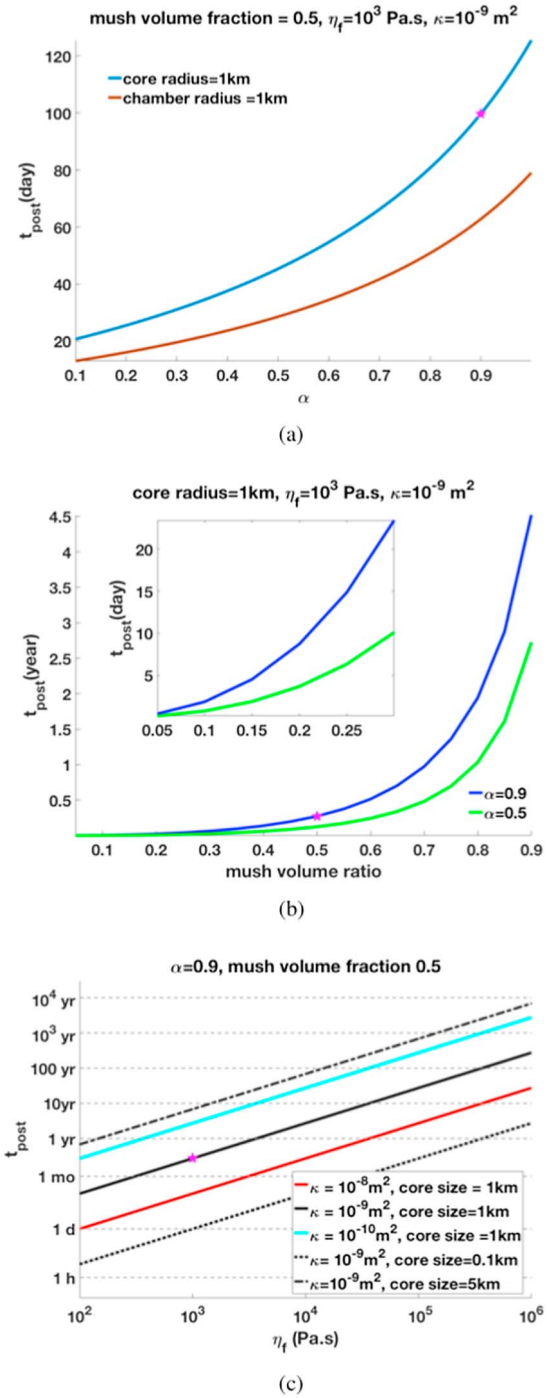

Figure 5. The postinjection evolution time t_{post} as a function of various system parameters, based on equation (A63) in Appendix A2.8. (a) The t_{post} as function of the poroelastic coefficient α for a chamber with 50% volume of mush. Blue and green curves correspond to a chamber with 1-km liquid core radius and 1 km of total radius, respectively. (b) The t_{post} as function of the mush volume fraction, for two cases with $\alpha = 0.5$ and 0.9, respectively. A zoom-in on small mush volume ratio is shown in the inset panel in (b). (c) The t_{post} as function of the magma viscosity η_f, for a system with $\alpha = 0.9$ and mush volume fraction of 0.5. The functions are shown for various combinations of mush permeability κ and liquid core size. In all panels, magenta stars correspond to the same combination of parameters with $\eta_f = 10^3$Pa s, $\kappa = 10^{-9}$ m^2, $\alpha = 0.9$, mush volume fraction 0.5, and a liquid core with 1-km radius. Other parameters are given in set #2 in Table A3.

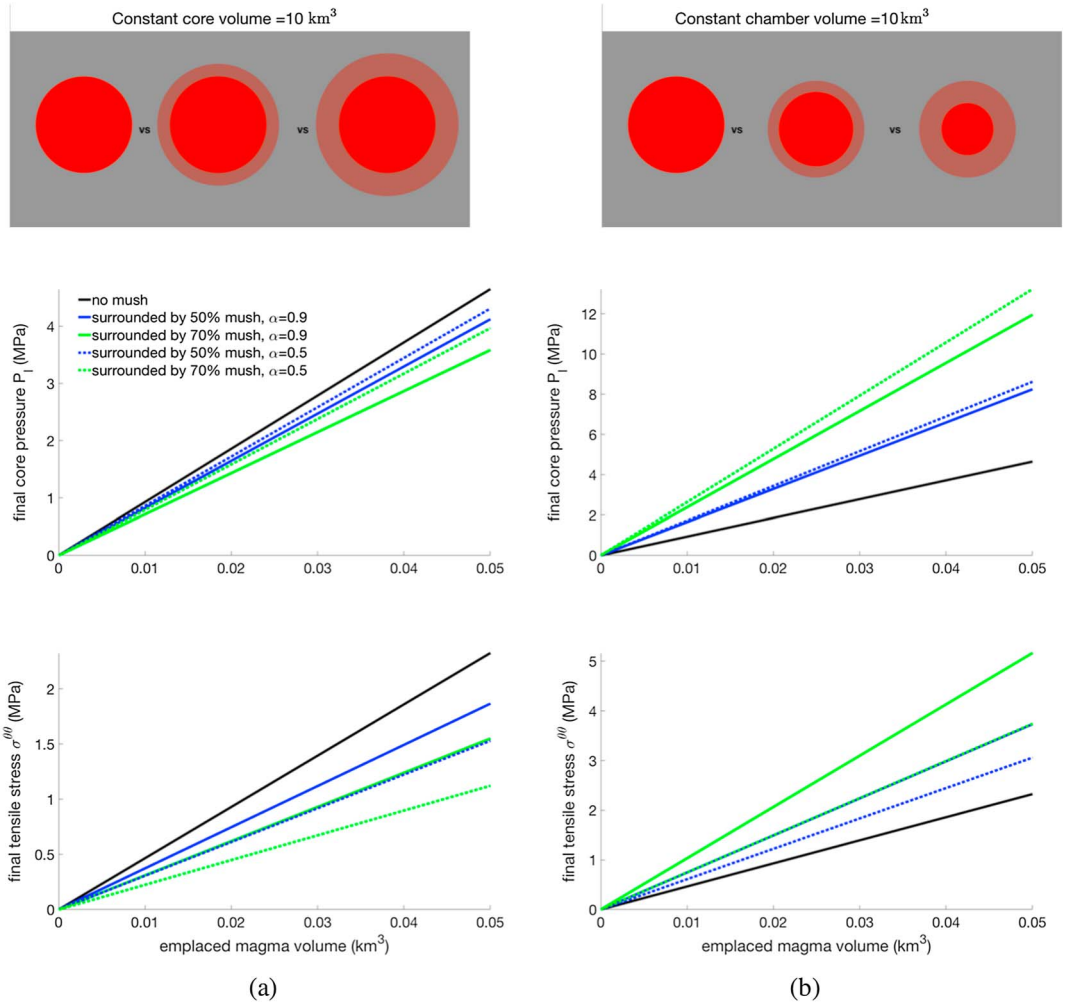

Figure 6. Postinjection steady state of the system, where core pressure and tensile stress are shown as functions of injected magma volume for different α and mush volume fraction in the chamber, assuming no rupture happens. The steady states are calculated analytically (see Appendix A2.8). The system has parameter set #2 in Table A3. Column (a) corresponds to a system with a core volume, wherein the total size of the chamber increases with the mush volume fraction; column (b) corresponds to a system with a total chamber volume, wherein the size of the core decreases with increasing mush volume fraction.

$t \rightarrow \infty$, are functions of the micromechanical parameters that also influence t_{post} (see section 3.2). As mentioned in section 3.2, the postinjection steady state is independent of the injection rate (Figures 4a and 4b). The postinjection steady state is also independent of the absolute value of R_o, κ, and η_f, which only affect the time it takes to reach the steady state. Although the physical arrangement of mush and melt within a magmatic system is not well constrained and likely to be complex (Caricchi & Blundy, 2015), we examine some simple cases to evaluate the importance of mush content on the final steady state of the system. By varying the volume fraction of mush (i.e., volume of mush shell divided by the total volume of the magma chamber), we find that the effect of mush content may influence the final steady state differently, depending on whether the core volume or the total chamber volume is held constant.

In one case, we hypothesize a series of magma chambers each with the same volume liquid core but an increasingly thick shell of surrounding mush. This case study reflects our ability to seismically detect liquid-filled bodies but the difficulty in resolving the amount of crystal mush or, in some cases, discerning it from hot country rock (e.g., Singh et al., 1998; Ward et al., 2014). With increasing mush shell thickness, the relative mush to liquid volume, hence the mush content, and the volume of the chamber increase. In this case, as the mush content increases, the same amount of injected magma causes lower core pressure and tensile stress. The end member of an elastic magma chamber model (i.e., no mush) results in the greatest increase in

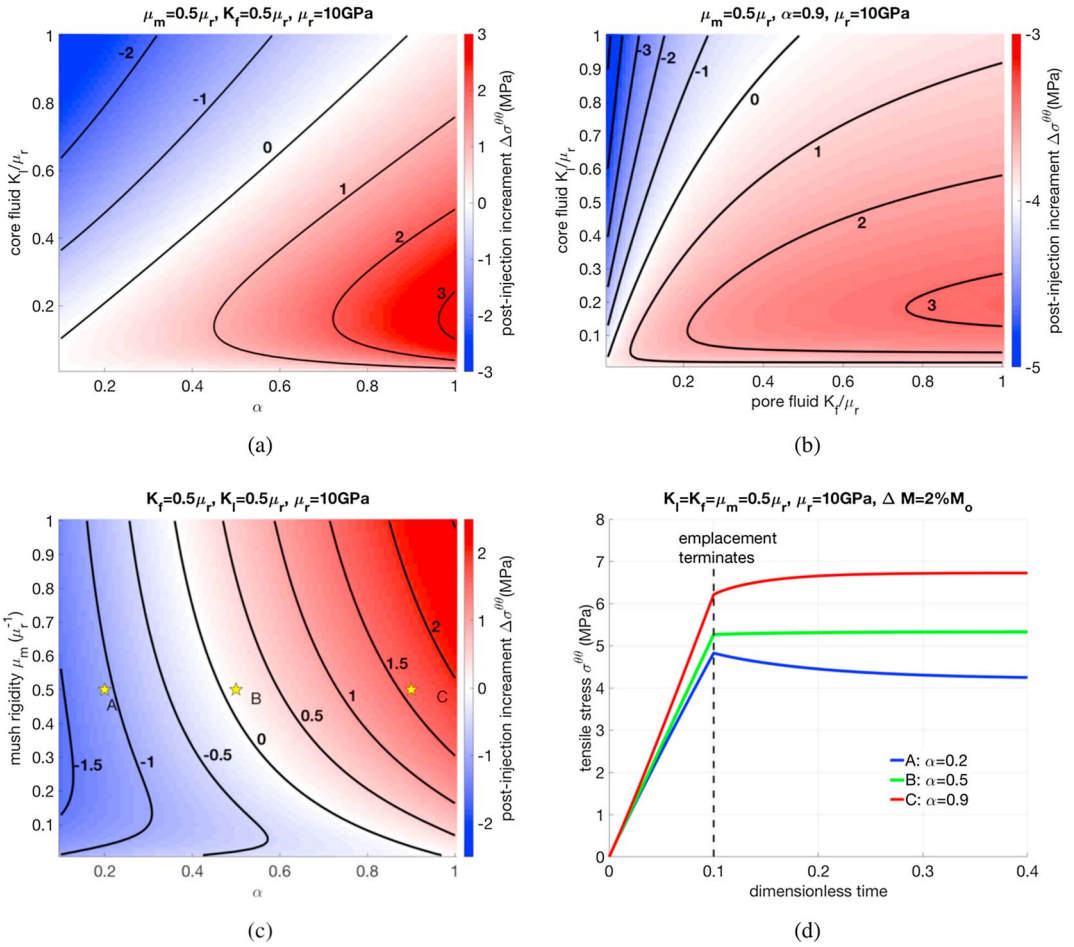

Figure 7. Postinjection change in tensile stress following a sudden injection for (a) $\mu_m = 0.5\mu_r, K_f = 0.5\mu_r$ and varying values of α and core fluid compressibility ($1/K_l$); (b) $\alpha = 0.9, \mu_m = 0.5\mu_r$ and varying values of pore fluid compressibility ($1/K_f$) and core fluid compressibility ($1/K_l$); and (c) $K_l = K_f = 0.5\mu_r$ and varying values of α and mush rigidity μ_m. The color red indicates that the tensile stress increases during the postinjection evolution (i.e., the magma chamber inflates); the color blue indicates that the tensile stress decreases during the postinjection evolution (i.e., the magma chamber deflates). Black lines are contours of normalized tensile stress increment. (d) Syninjection and postinjection evolution of the tensile stress for three cases, whose parameters are indicated on plot (c). Case A leads to a postinjection deflation (blue curve), case B leads to negligible postinjection tensile stress change (green curve), and case C leads to postinjection inflation (red curve), which we consider to be the most likely outcome for crystal mush. For all cases, ϕ_o, K_s, and R_o/r_o are given in parameter set # 1 in Table A3.

core pressure and tensile stress and hence has the highest likelihood of wall rock rupture for a given amount of injected magma (Figure 6 column a). In this case, the poroelastic mush functions as a buffer, allowing more magma to be injected before rupture happens, which is consistent with the findings of earlier, poroelastic chamber models (Gudmundsson, 2016). In another case, we hypothesize that the mushy chamber is formed from a liquid chamber by crystallization on the chamber walls (e.g., Marsh, 1989). With time, the mush shell becomes thicker and the liquid core volume decreases, while the total volume of the magma chamber remains constant. In this case, with increasing mush content, the same amount of injected mass causes increased core pressure and tensile stress (Figure 6 column b). In both cases, increasing the volume of injected magma causes a linear increase in the final core pressure and tensile stress, as is the case for the elastic (i.e., no mush) model. In addition to the relative proportions of mush and magma, the poroelastic coefficient of the mush (α) also strongly influences the final steady state of the system. A higher value of α (i.e., relatively weak pore structure) makes the mush shell more *leaky*, which reduces the core pressure by increasing core-to-mush magma transport. Higher value of α also causes the mush shell to swell more, leading to higher tensile stress in the host rock (Figures 7 and A4). Other micromechanical quantities, such as the relative compressibility of magma and rigidity of the mush, influence the final steady state to a lesser degree (see Appendix A2.9, Figure A4).

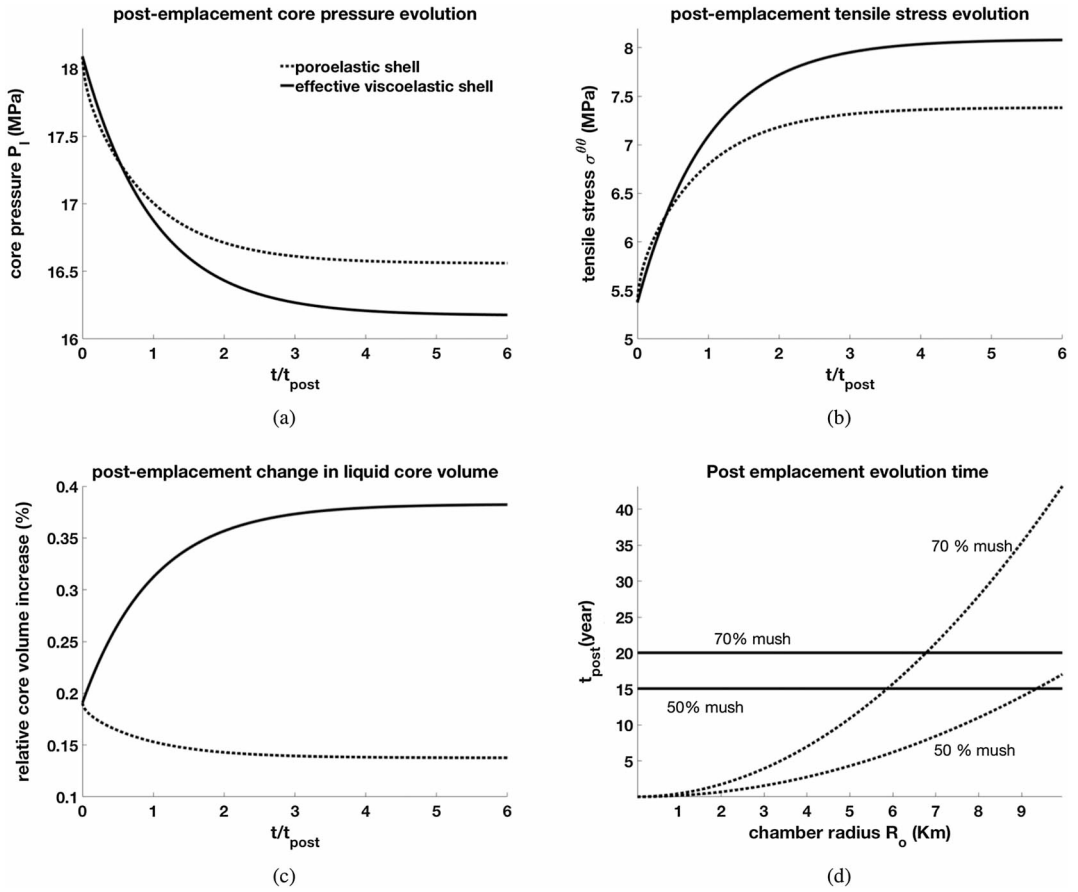

Figure 8. Diffusion and relaxation processes following sudden injection of $\Delta M = 2\% M_o$ for a system with a poroelastic mush shell (dashed line) and a system with an effective viscoelastic shell (solid line). (a–c) The postinjection evolution of liquid core pressure, rock tensile stress, and the volume change of the liquid core for mush volume fraction of 50%. The postinjection time (x axis) is normalized by the postinjection evolution time t_{post} for the poroelastic shell and t_{post}^{visc} for the viscoelastic shell, respectively (see Appendix A3). (d) The postinjection evolution time t_{post} (or t_{post}^{visc}, for the viscoelastic cases), as functions of the total size of the magma chamber, for two different mush volume fraction. To calculate t_{post} or t_{post}^{visc}, we assume magma viscosity $\mu_f = 10^3$ Pa s and mush permeability $\kappa = 10^{-9}$ m^2 for the poroelastic mush and assume the viscosity of the crystalline framework $\eta_m = 10^{18}$ Pa s following Segall (2016). Other parameters are given in set #3 in Table A3.

As discussed in section 3.1, during the postinjection evolution, the pressure in the liquid core always decreases (Figure 4a) due to diffusion of magma into the mush, regardless of its specific micromechanical properties of the mush. However, the postinjection evolution of the tensile stress in the host rock (i.e., the total volume of the magma chamber) may increase, decrease, or remain constant, depending on the specific system (Figure 7d). Using the analytical solution for the end member of an instantaneous injection (see Appendix A2.9), we find that how the tensile stress evolves after the injection depends on a combination of different micromechanical properties. Specifically, the tensile stress is more likely to increase (i.e., the postinjection increment $\Delta\sigma_{rock}^{\theta\theta} > 0$ in Figures 7a–7c) if the pore structure is significantly weaker than the solid crystals (i.e., corresponding to large α value), if the fluids in the core are relatively compressible, or if the mush ensemble is relatively rigid to shearing (i.e., moderate μ_m).

5. Poroelastic Versus Viscoelastic Response

Transient evolution in a magma chamber after an injection is not strictly poroelastic response but can also be caused by viscoelastic deformation, as suggested in previous research (Dragoni & Magnanensi, 1989; Jellinek & DePaolo, 2003; McTigue, 1987; Nooner & Chadwick, 2009; Segall, 2016). Here we explore a case where the mush behaves effectively as a viscoelastic material. We consider the rheology of poroviscoelasticity involving a short viscoelastic relaxation time and a long poroelastic diffusion time (e.g., if the magma viscosity is

very high, or if the mush has very low permeability). In this end member case, the mush shell remains in an undrained condition during the viscoelastic relaxation of the crystalline matrix (i.e., the pore magma is always locked in the interstitial spaces). The deformation of the mush shell is therefore equivalent to a viscoelastic shell, which we then approximate as a Maxwell solid. We apply a Laplace transform on the poroelastic solution in an undrained condition (see Appendix A3), similar to the approach for comparable viscoelastic models (Dragoni & Magnanensi, 1989; Segall, 2016). Comparing the postinjection evolution of the viscoelastic case with the poroelastic model, we find that both models involve a postinjection decrease in the liquid core pressure and increase in the tensile stress in the host rock (Figures 8a and 8b). However, the postinjection evolution of the volume of the liquid core follows opposite trends for the two models. In the poroelasitc model, the transport of magma from the core to the shell causes the liquid core volume and core pressure to decrease, whereas in the viscoelastic model, the outward *creeping* of mush shell (i.e., both the liquid-mush boundary and the mush-rock boundary push outward) causes the core volume to increase and the core pressure to decrease (Figure 8c). It is also worth noting that, contrary to the postinjection poroelastic evolution time t_{post} (as discussed in section 3.2), which depends sensitively on the total size of the chamber ($t_{post} \propto R_o^2$), the characteristic viscoelastic postinjection evolution time t_{post}^{visc} depends only on the ratio r_o/R_o. Hence, for a given mush volume fraction, t_{post}^{visc} is independent of the total size of the magma chamber (see Appendix A3 and Figure 8d). These differences between the two models, particularly the size dependence of the postinjection transient evolution, can potentially provide a means to determine which rheology is responsible for the observed transient deformation in volcanic systems.

6. Summary and Conclusions

In this study, we develop an analytical model to evaluate how the abundance of crystal mush influences the mechanical evolution of crustal magmatic systems. By assuming a spherical magma chamber consisting a liquid core enveloped by a mush shell, we explore the behavior of the magma-mush-rock system during and after a magma injection event. We find that when the mush behaves poroelastically, the system continues to evolve after the injection of magma has terminated. Porous flow from the liquid core into the mush shell causes the pressure in the liquid magma core to decrease during the postinjection evolution. Expansion of the mush shell due to added pore pressure often causes the system to reach maximum tensile stresses at some time after the injection has already ceased. For a liquid magma core of given volume, a thicker mush shell (higher mush-melt ratio) acts as a buffer, decreasing the final core pressure and the tensile stress. As a result, more mush can potentially allow more liquid magma to be injected before a chamber ruptures. We find that the poroelastic coefficient α of the crystal mush and the volume fraction of mush in the chamber play important roles in determining the postinjection steady state of the system. In addition, chamber dimension, magma viscosity, and mush permeability exert a strong control on the time scale of the postinjection evolution. The importance of the parameters such as the poroelastic coefficient, magma viscosity, and mush permeability on the transient evolution and/or the final steady state of mushy systems demonstrates the need for further investigation of the micromechanical properties of crystal mush.

We compare the above poroelastic syninjection and postinjection evolution with model predictions using a viscoelastic rheology for the mush shell and using an elastic model (i.e., no mush). Both poroelastic and viscoelastic mush shells result in postinjection transient evolution, in contrast to the mushless case, wherein the magma chamber achieves a new steady state immediately when the injection ceases. The poroelastic and viscoelastic models display some similar behaviors as both can yield a postinjection increase in tensile stress and decrease in core pressure. However, a notable difference between the models is that the poroelastic postinjection evolution time depends on the size of the magma chamber, while the time scale of the postinjection viscoelastic response, for a fixed mush volume fraction (i.e., the ratio r_o/R_o), is independent of the absolute size of the chamber. This difference may provide a means to distinguish which rheology (poroelasticity or viscoelasticity) is dominant for natural magmatic systems where the time scales and magnitudes of transient evolutions can be observed through geodetic measurements. However, we recognize that for such comparisons, the described models would require further development, including incorporation of a free surface to model deformation and exploration of nonradially symmetric geometries both in the dimensions of the magma chamber and distribution of the mush within it.

In this first step for considering the mechanical effects of poroelastic mush in a magma chamber, one of the key findings is that magma is transferred from the liquid core to surrounding mush. The ability of a poroelastic

mush shell to store magma has important potential implications when a mushy chamber is a part of a larger magmatic plumbing system. For example, during an injection event, the injection rate is typically assumed to be proportional to the difference between a shallow magma chamber and deep magmatic reservoir with higher pressure P_{deep} (Mastin et al., 2008; Segall, 2016). In the case of a mushy, shallow chamber, porous flow from the core into the mush shell will decrease the chamber pressure, maintaining a larger-pressure difference $P_{deep} - P_l$ and allowing more magma to be injected into the shallow mushy chamber. Conversely, when a mushy chamber discharges magma to the surface, the overpressure between the chamber and the lithosphere $P_l - P_{lith}$ controls the discharge rate. In this case, the decrease in core pressure can draw the pore magma back into the core and hence maintain a higher overpressure, potentially leading to longer discharge time, and more magma erupted. Thus, understanding the properties of mushy magmatic systems, and especially whether the mush behaves as a poroelastic material, will be essential in order to improve our models of the behavior and potential hazards posed by volcanism.

Appendix A: Theoretical Framework

The variables in our study are defined in Table A1, which vary with space (radial position r) or time t. The constant parameters are shown in Table A2.

A1. Model Setup

We assume that the system is initially at a steady state, with uniform liquid pressure in both the core magma and the pore fluids in the mush shell. At time $t = 0^+$, an injection begins and causes the system to deviate from its initial equilibrium state. We define subscripts $_{(0)}$ to refer to the preinjection equilibrium state and define radial position r as the distance from the center of the magma chamber to the equilibrium position of any given element in the mush shell or host rock and t as time (see Table A1). Following the onset of the injection, the new displacements in the system become $\vec{u}_{m,(0)}(r) + \vec{u}_m(r,t)$ (in the mush) and $\vec{u}_{\text{rock},(0)}(r) + \vec{u}_{\text{rock}}(r,t)$ (in the rock); the stresses become $\boldsymbol{\sigma}_{m,(0)}(r) + \boldsymbol{\sigma}_m(r,t)$ (in the mush) and $\boldsymbol{\sigma}_{\text{rock},(0)}(r) + \boldsymbol{\sigma}_{\text{rock}}(r,t)$ (in the rock); the core pressure and pore pressure become $P_{l,(0)} + P_l(t)$ and $P_{f,(0)} + P_f(r,t)$, respectively. We assume that the deformations in the mush shell and host rock obey the constitutive relations for linear poroelastic and elastic solids. By linearizing the system, we can show that the increments $\vec{u}_m$, $\vec{u}_{\text{rock}}$, $\boldsymbol{\sigma}_m$, $\boldsymbol{\sigma}_{\text{rock}}$, P_l, and P_f obey (Cheng, 2016; Biot, 1941; Landau & Lifshitz, 1959; Rice & Cleary, 1976)

$$\boldsymbol{\sigma}_{\text{rock}} = (K_r - \frac{2}{3}\mu_r)\nabla \cdot \vec{u}_{\text{rock}}\boldsymbol{I} + \mu_r\left(\nabla\vec{u}_{\text{rock}} + \nabla\vec{u}_{\text{rock}}^T\right) \tag{A1a}$$

$$\boldsymbol{\sigma}_m = (K_m - \frac{2}{3}\mu_m)\nabla \cdot \vec{u}_m\boldsymbol{I} + \mu_m\left(\nabla\vec{u}_m + \nabla\vec{u}_m^T\right) - \alpha P_f\boldsymbol{I}, \tag{A1b}$$

Table A1
Variables in the System

	Symbol	Definition
variables	r	equilibrium radial distance of a given element
	t	time, measured from the beginning of the magma injection
	$\vec{u}_m(r,t)$	displacement increment in mush shell
	$\vec{u}_{\text{rock}}(r,t)$	displacement increment in host rocks
	$\boldsymbol{\sigma}_m$, $\sigma_m^{rr}(r,t)$	increments in poroelastic stress and its radial component in the mush
	$\boldsymbol{\sigma}_{\text{rock}}$, $\sigma_{\text{rock}}^{rr}$, $\sigma_{\text{rock}}^{\theta\theta}(r,t)$	increments in elastic stress, its radial, and its tensile components in host rock
	$P_f(r,t)$	pore fluid pressure increment in mush shell
	$P_l(t)$	liquid core pressure increment
	$m(r,t)$	variation in pore fluid content in the mush
	$M_{\text{leak}}(t)$	mass of magma transported from core into mush from time 0 to t
	$\vec{q}(r,t)$	Darcy's velocity in mush shell
	$\rho_f(r,t)$	pore fluid density increment in mush shell
	$M_{\text{inj}}(t)$	mass injected into the liquid core from time 0 to t
	$\phi(r,t)$	porosity change in mush shell

Table A2
Symbols of the Constants Used in the Study

	Symbol	Definition	Typical value/expression
constants	r_o	radius of liquid magma core at initial steady state	0.1–5 km
	R_o	radius of magma chamber at initial steady state	$2r_o$
	α	poroelastic coefficient (Biot coefficient)	0.5, 0.9
	c	poroelastic diffusivity	$\frac{\kappa}{\eta_f}\frac{(K_m+\frac{4}{3}\mu_m)(K_u-K_m)}{\alpha^2(K_u+\frac{4}{3}\mu_m)}$
	K_m	drained bulk modulus of mush	$(1-\alpha)K_s$
	K_u	undrained bulk modulus of mush	$(1-\alpha)K_s+\frac{\alpha^2K_sK_f}{\phi_oK_s+(\alpha-\phi_o)K_f}$
	K_r	elastic bulk modulus of host rock	$\frac{5}{3}\mu_r$
	K_l	bulk modulus of pore fluid	$0.01\mu_r-\mu_r$
	K_f	bulk modulus of core magma	$0.01\mu_r-\mu_r$
	μ_r	shear modulus (rigidity) of host rock	10GPa
	μ_m	shear modulus (rigidity) of mush ensemble	$0.01\mu_r-\mu_r$
	$\rho_{f,(0)}$	magma density at initial steady state	value not used
	η_f	viscosity of pore magma	10^2-10^6Pa.s
	η_m	viscosity of the mush ensemble	10^{18}Pa.s
	κ	permeability in mush	$10^{-10}-10^{-8}m^2$
	ϕ_o	porosity in mush at initial steady state	0.2
	M_o	total mass in the liquid core before injection	value not used
	ΔM	total mass injected into the chamber	$0.02\%M_o$
	t_{inj}	injection time (normalized)	0.01, 0.1, 0.5 (normalized)
	r_{inj}	injection rate	$\frac{\Delta M}{t_{\text{inj}}}\left(1-H(t-t_{\text{inj}})\right)$
	t_{post}	postinjection evolution time scale (poroelastic case)	solved from model
	$t_{\text{post}}^{\text{vist}}$	postinjection evolution time scale (viscoelastic case)	solved from model
	τ_{system}	factor in $t_{\text{post}}=\tau_{\text{system}}\tau_m$ with unit of time	$\frac{R_o^2\eta_f}{\kappa\mu_r}$
	τ_m	dimensionless factor in $t_{\text{post}}=\tau_{\text{system}}\tau_m$	solved from model

where material constants K_r, μ_r, K_m, μ_m, and α are defined in Table A2 and discussed in section 2.3.1. As discussed in section 2.3.1, we assume an intermediate to large value of α (close to 1) in the crystal mush.

We define the variation in pore fluid content $m(r,t)$ by the pore fluid mass gained or lost per unit undeformed volume of mush (Biot, 1941; Cheng, 2016), which has units of density. Considering isothermal compression/dilation of the pore fluid, we approximate m using the linear relation (Biot, 1941; Cheng, 2016; Rice & Cleary, 1976)

$$m=\rho_{f,(0)}\alpha\left(\nabla\cdot\vec{u}_m+\frac{\alpha}{K_u-K_m}P_f\right) \tag{A2}$$

and assume the undrained bulk modulus of the mush is (see Table A2 and Cheng, 2016):

$$K_u=(1-\alpha)K_s+\frac{\alpha^2K_sK_f}{\phi_oK_s+(\alpha-\phi_o)K_f} \tag{A3}$$

Table A3
Parameters Used in Computations for Figures in the Main Text

Parameter combination	α	$\frac{R_o}{r_o}$	ϕ_0	$\frac{K_s}{\mu_r}$	$\frac{K_f}{\mu_r}$	$\frac{K_l}{\mu_r}$	$\frac{\mu_m}{\mu_r}$	$\frac{\Delta M}{m_0}$
1	0.9	2	0.2	5/3	0.5	0.1	1	0.02%
2	[a]	[a]	0.2	5/3	0.5	0.1	0.5	[b]
3	0.9	2	0.2	5/3	0.5	0.5	0.5	0.02%

[a]denotes that the parameter is varied in the computation. [b]denotes that the parameter is irrelevant to the computation.

m can be integrated across the mush shell to yield the total amount of magma gained or lost by the mush shell M_{leak}:

$$M_{\text{leak}}(t) = 4\pi \int_{r_o}^{R_o} m(r,t) r^2 \mathrm{d}r. \tag{A4}$$

According to the definition of m, $M_{\text{leak}} > 0$ indicates that magma is transported (i.e., *leaked*) from the liquid core into the mush shell.

A2. Governing Equation for Syninjection and Postinjection Evolution

A2.1. Pressure and Mass in the Liquid Core

The injection of magma causes the pressure in the liquid core to increase, which can be calculated if the injection rate is known. In our study, we assume that the injection occurs over the time period $0 \le t \le t_{\text{inj}}$, during which magma with total mass ΔM is added into the core at a constant mass flow rate. At $t = t_{\text{inj}}$, the injection terminates. The injection rate, defined as the mass injected into the liquid core per unit time, is

$$r_{\text{inj}} = \frac{\Delta M}{t_{\text{inj}}} \left(1 - H(t - t_{\text{inj}})\right), \qquad \text{when} \quad t_{\text{inj}} > 0, \tag{A5}$$

where H is the Heaviside function (i.e., $H(t-t_{\text{inj}}) = 0$ for $t - t_{\text{inj}} < 0$ and $H(t-t_{\text{inj}}) = 1$ for $t - t_{\text{inj}} > 0$). We can verify that $r_{\text{inj}} = \Delta M / t_{\text{inj}}$ during the injection and $r_{\text{inj}} = 0$ after the injection. When the injection is very rapid and $t_{\text{inj}} \to 0$, the end member case corresponds to an instantaneous injection with injection rate $r_{\text{inj}} = \Delta M \delta(0)$, where δ is the Dirac delta function. At any time t, we define M_{inj} to be the total amount of magma that has been added into the chamber from time 0 to t:

$$M_{\text{inj}}(t) = \int_0^t r_{\text{inj}}(t') \mathrm{d}t'. \tag{A6}$$

Substituting (A5) into (A6), M_{inj} becomes

$$M_{\text{inj}}(t) = \begin{cases} \frac{\Delta M}{t_{\text{inj}}} \left(t - (t - t_{\text{inj}}) H(t - t_{\text{inj}})\right), & t_{\text{inj}} > 0 \\ \Delta M, & t_{\text{inj}} = 0, \end{cases} \tag{A7}$$

where the lower case corresponds to the end member of an instantaneous injection. We can verify that M_{inj} increases linearly with time during the injection and holds a constant value $M_{\text{inj}} = \Delta M$ after the injection terminates. At time t, the total increase of magma in the liquid core $\Delta M_{\text{core}}(t) = M_{\text{inj}}(t) - M_{\text{leak}}(t)$ then becomes

$$\Delta M_{\text{core}}(t) = \begin{cases} \frac{\Delta M}{t_{\text{inj}}} \left(t - (t - t_{\text{inj}}) H(t - t_{\text{inj}})\right) - 4\pi \int_{r_o}^{R_o} m(r,t) r^2 \mathrm{d}r, & t_{\text{inj}} > 0 \\ \Delta M - 4\pi \int_{r_o}^{R_o} m(r,t) r^2 \mathrm{d}r, & t_{\text{inj}} = 0. \end{cases} \tag{A8}$$

The increase in core fluid mass $\Delta M_{\text{core}}(t)$ can also be approximated using linear expansion:

$$\begin{aligned} \Delta M_{\text{core}}(t) &= V_{\text{core},(0)} \Delta \rho_{\text{core}}(t) + \rho_{\text{core},(0)} \Delta V_{\text{core}}(t) \\ &= \left(\frac{4\pi}{3} r_o^3\right) \left(\frac{P_l(t)}{K_l} \rho_{\text{core},(0)}\right) + \rho_{\text{core},(0)} \left(4\pi r_o u_m(r_o, t)\right), \end{aligned} \tag{A9}$$

where the $\rho_{\text{core},(0)} = \rho_{f,(0)}$ is the preinjection magma density, $V_{\text{core},(0)} = \frac{4}{3}\pi r_o^3$ is the preinjection core volume, K_l is the bulk modulus of the core fluid during isothermally compression, and $u_m(r_o, t)$ is the radial displacement of the boundary between the liquid core and the mush shell. Substituting (A8) into (A9), the core pressure increment $P_l(t)$ becomes

$$P_l(t) = \begin{cases} K_l \left(\frac{\Delta M}{M_o t_{\text{inj}}} \left(t - (t - t_{\text{inj}}) H(t - t_{\text{inj}})\right) - \frac{4\pi}{M_o} \int_{r_o}^{R_o} m(r,t) r^2 \mathrm{d}r - \frac{3 u_m(r_o,t)}{r_o} \right), & t_{\text{inj}} > 0 \\ K_l \left(\frac{\Delta M}{M_o} - \frac{4\pi}{M_o} \int_{r_o}^{R_o} m(r,t) r^2 \mathrm{d}r - \frac{3 u_m(r_o,t)}{r_o} \right), & t_{\text{inj}} = 0. \end{cases} \tag{A10}$$

A2.2. Deformation in Country Rock

The country rock surrounding the magma chamber is modeled as an infinite domain of elastic solid, whose deformation is described by the constitutive relation (A1a). Assuming radial symmetry, the displacement in the country rock during and after the injection only has a radial component $\vec{u}_{\text{rock}} = u_{\text{rock}}(r,t)\hat{r}$ $(r \geq R_o)$, where $\hat{r}$ is the unit vector along the radial direction. Assuming a quasi-static state in the country rock $\nabla \cdot \boldsymbol{\sigma}_{\text{rock}} = 0$ at all time, we obtain

$$\left(K_r - \frac{2}{3}\mu_r\right)\nabla\left(\nabla \cdot \vec{u}_{\text{rock}}\right) + \mu_r\left(\nabla^2\vec{u}_{\text{rock}} + \nabla\left(\nabla \cdot \vec{u}_{\text{rock}}\right)\right) = 0. \tag{A11}$$

Using the relation $\nabla^2\vec{u}_{\text{rock}} = \nabla\left(\nabla \cdot \vec{u}_{\text{rock}}\right) - \nabla\times\nabla\times\vec{u}_{\text{rock}}$ and considering the radial symmetry (i.e., $\nabla\times\vec{u}_{\text{rock}} = 0$), the equilibrium condition $\nabla \cdot \boldsymbol{\sigma}_{\text{rock}} = 0$ leads to

$$\frac{\partial}{\partial r}\left(r^2\frac{\partial}{\partial r}\left(r^2 u_{\text{rock}}(r,t)\right)\right) = 0, \tag{A12}$$

which has solution for the displacement and stress components

$$u_{\text{rock}}(r,t) = \frac{C(t)R_o^3}{r^2}, \quad \sigma^{rr}_{\text{rock}}(r,t) = \frac{-4\mu_r C(t)R_o^3}{r^3}, \quad \sigma^{\theta\theta}_{\text{rock}}(r,t) = \sigma^{\phi\phi}_{\text{rock}}(r,t) = \frac{2\mu_r C(t)R_o^3}{r^3}, \tag{A13}$$

where $C(t)$ is an unknown dimensionless function in time and $\sigma^{rr}_{\text{rock}}$ and $\sigma^{\theta\theta}_{\text{rock}}$ are the radial and tensile components of the elastic stress. We assume that the stresses and deformation in the host rock vanish at infinity.

A2.3. Deformation and Fluid Transport in Mush Shell

We assume the mush to be an ideal poroelastic material, whose displacement $\vec{u}_m = u_m\hat{r}$ and stress $\boldsymbol{\sigma}_m$ are described by the constitutive relation (A1b) (Cheng, 2016). Assuming quasi-static state $\nabla \cdot \boldsymbol{\sigma} = 0$ and radial symmetry (i.e., $\nabla \times \vec{u}_m = 0$), we obtain

$$\nabla\left((K_m + \frac{4}{3}\mu_m)\nabla \cdot \vec{u}_m - \alpha P_f\right) = 0, \tag{A14}$$

which indicates that the combination of volumetric strain and pore pressure $(K_m + \frac{4}{3}\mu_m)\nabla \cdot \vec{u}_m(r,t) - \alpha P_f(r,t)$ only varies with time. Taking the gradient of the equilibrium condition (A14) and the constitutive relation (A2), respectively, we obtain the relation between $P_f(r,t)$ and the variation in fluid content $m(r,t)$:

$$\nabla P_f = \frac{(K_m + \frac{4}{3}\mu_m)(K_u - K_m)}{\alpha^2\rho_{f,(0)}(K_u + \frac{4}{3}\mu_m)}\nabla m. \tag{A15}$$

We assume that the motion of the pore magma in the permeable mush obeys the Darcy's law and the conservation of mass:

$$\vec{q} + \frac{\kappa}{\eta_f}\nabla P_f = 0 \tag{A16a}$$

$$\frac{\partial}{\partial t}m(r,t) + \rho_{f,(0)}\nabla \cdot \vec{q} = 0, \tag{A16b}$$

where $\vec{q}$ is the Darcy's velocity, η_f is the viscosity of the magma in the pore space, and κ is the permeability of the mush, here assumed to be uniform in space and constant in time. Taking the gradient of (A16a) and combine it with (A16b) and (A15), we obtain a diffusion type equation for m

$$\frac{\partial}{\partial t}m - c\nabla^2 m = 0 \tag{A17}$$

where c is the effective diffusivity

$$c = \frac{\kappa}{\eta_f}\frac{(K_m + \frac{4}{3}\mu_m)(K_u - K_m)}{\alpha^2(K_u + \frac{4}{3}\mu_m)}. \tag{A18}$$

Therefore, the porous magma flow in the quasi-static mush shell is described by the diffusion of the variance in fluid content m.

A2.4. Boundary Conditions

During the injection, we assume that rapid elastic deformation can always maintain a force balance on the fluid-mush interface and mush-solid interface. We also assume that the deformation is continuous on the mush-rock interface and that the mush-rock boundary is impermeable to magma (ie., no magma is allowed to *leak* into the host rock). These assumptions lead to the conditions on the inner boundary $r = r_o$ and outer boundary $r = R_o$:

$$\sigma_m^{rr}(r_o, t) + P_l(t) = 0 \tag{A19a}$$

$$\sigma_m^{rr}(R_o, t) - \sigma_{\text{rock}}^{rr}(R_o, t) = 0 \tag{A19b}$$

$$\nabla P_f(R_o, t) = 0 \tag{A19c}$$

$$u_m(R_o, t) - u_{\text{rock}}(R_o, t) = 0 \tag{A19d}$$

$$P_l(t) - P_f(r_o, t) = 0, \qquad (t > 0), \tag{A19e}$$

where (A19a) and (A19b) describe the force balances on the inner and outer boundary of the mush shell, respectively, (A19c) indicates that the porous flows must vanish at the mush-rock interface, and (A19d) describes the continuity of radial displacement at the mush-rock boundary. The last condition (A19e) describes the continuity in fluid pressure at the fluid-mush boundary, which is satisfied unless when $t = 0$ for an instantaneous injection, in which case the sudden compression of the core fluid causes an instantaneous pressure discontinuity across the core-mush boundary. Given the solutions for the deformation in the host rock (A13), the boundary values of u_{rock} and $\sigma_{\text{rock}}^{rr}$ satisfy the relation $-4\mu_r \frac{u(R_o,t)}{R_o} = \sigma^{rr}(R_o, t)$, which is substituted into (A19b) and (A19d) to obtain the relation

$$-4\mu_r \frac{u_m(R_o, t)}{R_o} = \sigma_m^{rr}(R_o, t). \tag{A20}$$

A2.5. Dimensionless Governing Equations and Boundary Conditions

For convenience and better interrogation of the parameter space, we nondimensionalize the quantities in the fluid-mush-rock system using the length scale L^*, pressure/stress scale $\boldsymbol{\sigma}^*$, time scale t^*, and the scale for the variation of fluid content (i.e., density) m^*, which are

$$L^* = R_o, \qquad \boldsymbol{\sigma}^* = \mu_r, \qquad t^* = \frac{R_o^2}{c} \qquad m^* = \rho_{f,(0)}.$$

The time scale is determined by the diffusivity c defined in (A18). Using the scales above, the quantities in the system are normalized, such that

$$r \to \frac{r}{L^*}, \qquad u_{m,\text{rock}} \to \frac{u_{m,\text{rock}}}{L^*}, \qquad t \to \frac{t}{t^*}, \qquad P_{l,f} \to \frac{P_{l,f}}{\boldsymbol{\sigma}^*}, \qquad \boldsymbol{\sigma}_{m,\text{rock}} \to \frac{\boldsymbol{\sigma}_{m,\text{rock}}}{\boldsymbol{\sigma}^*}, m \to \frac{m}{m^*}$$

where $u_{m,\text{rock}}$ and $\boldsymbol{\sigma}_{m,\text{rock}}$ indicate the displacement and stress in either the mush shell or the crust rock and $P_{l,f}$ indicates the fluid pressure in either the core or the pore spaces. Using the normalized quantities, the dimensionless diffusion equation for the dimensionless variation in fluid content m becomes

$$\frac{\partial}{\partial t} m - \nabla^2 m = 0 \tag{A21}$$

and the constitutive relation (A2) leads to the relation between the dimensionless quantities

$$m(r, t) = \alpha \left(\nabla \cdot \vec{u}_m(r, t) + \frac{\alpha}{\frac{K_u}{\mu_r} - \frac{K_m}{\mu_r}} P_f(r, t) \right) \tag{A22}$$

where $\nabla \cdot \vec{u}_m$ and P_f are further related by the dimensionless form of the equilibrium condition (A14)

$$\frac{\partial}{\partial r} \left(\left(\frac{K_m}{\mu_r} + \frac{4}{3} \frac{\mu_m}{\mu_r} \right) \nabla \cdot \vec{u}_m - \alpha P_f \right) = 0. \tag{A23}$$

As $\left(\frac{K_m}{\mu_r}+\frac{4}{3}\frac{\mu_m}{\mu_r}\right)\nabla\cdot\vec{u}_m-\alpha P_f$ does not vary in space, we define a dimensionless function in time $\zeta(t)$, such that

$$\zeta(t)=\left(\frac{K_m}{\mu_r}+\frac{4}{3}\frac{\mu_m}{\mu_r}\right)\nabla\cdot\vec{u}_m-\alpha P_f. \tag{A24}$$

The combination of (A22) and (A24) leads to

$$\nabla\cdot\vec{u}_m(r,t)=\frac{K_u-K_m}{\alpha(K_u+\frac{4}{3}\mu_m)}m(r,t)+\frac{\mu_r}{K_u+\frac{4}{3}\mu_m}\zeta(t) \tag{A25a}$$

$$P_f=\frac{(K_m+\frac{4}{3}\mu_m)(K_u-K_m)}{\alpha^2\mu_r(K_u+\frac{4}{3}\mu_m)}m(r,t)-\frac{K_u-K_m}{\alpha(K_u+\frac{4}{3}\mu_m)}\zeta(t). \tag{A25b}$$

In (A25a), the divergence $\nabla\cdot\vec{u}_m=\frac{1}{r^2}\frac{\partial}{\partial r}(r^2u_m)$ can be integrated to obtain u_m

$$u_m(r,t)=\frac{u_m(1,t)}{r^2}-\frac{1}{r^2}\frac{K_u-K_m}{\alpha(K_u+\frac{4}{3}\mu_m)}\int_r^1 r'^2m(r',t)\mathrm{d}r'-\frac{\mu_r}{K_u+\frac{4}{3}\mu_m}\frac{\zeta(t)}{3}(\frac{1}{r^2}-r), \tag{A26}$$

where $u_m(1,t)$ is the radial displacement of the mush-rock interface (i.e., at normalized radial position $r=1$). With radial symmetry, the dimensionless radial component σ_m^{rr}, according to the constitutive relation (A1b), becomes

$$\sigma_m^{\mathrm{rr}}=\left(\frac{K_m}{\mu_r}+\frac{4}{3}\frac{\mu_m}{\mu_r}\right)\nabla\cdot\vec{u}_m-4\frac{\mu_m}{\mu_r}\frac{u_m}{r}-\alpha P_f, \tag{A27}$$

which is further expressed using (A25a) and (A26)

$$\sigma_m^{\mathrm{rr}}(r,t)=\zeta(t)-\frac{4u_m(1,t)\mu_m}{r^3\mu_r}+\frac{4\mu_m}{r^3\mu_r}\frac{K_u-K_m}{\alpha(K_u+\frac{4}{3}\mu_m)}\int_r^1 r'^2m(r',t)\mathrm{d}r'+\frac{4\mu_m}{K_u+\frac{4}{3}\mu_m}\frac{\zeta(t)}{3}(\frac{1}{r^3}-1). \tag{A28}$$

Inside the liquid core, the dimensionless core pressure (A10) becomes

$$P_l(t)=\begin{cases}\frac{K_l}{\mu_r}\left(\frac{\Delta M}{M_o t_{\mathrm{inj}}}\left(t-(t-t_{\mathrm{inj}})H(t-t_{\mathrm{inj}})\right)-3\left(\frac{R_o}{r_o}\right)^3\int_{r_o/R_o}^1 r'^2m(r',t)\mathrm{d}r'-3\frac{R_o}{r_o}u_m(\frac{r_o}{R_o},t)\right)\\ \frac{K_l}{\mu_r}\left(\frac{\Delta M}{M_o}-3\left(\frac{R_o}{r_o}\right)^3\int_{r_o/R_o}^1 r'^2m(r',t)\mathrm{d}r'-3\frac{R_o}{r_o}u_m(\frac{r_o}{R_o},t)\right),\end{cases} \tag{A29}$$

where the injection time period t_{inj} in the upper case is normalized by the diffusion time scale and the lower case corresponds to the end member of a sudden injection. Outside of the magma chamber, the dimensionless solutions (A13) for the radial displacement and stress in the country rock become

$$u_{\mathrm{rock}}(r,t)=\frac{C(t)}{r^2},\qquad \sigma_{\mathrm{rock}}^{\mathrm{rr}}(r,t)=-4\frac{C(t)}{r^3},\qquad \sigma_{\mathrm{rock}}^{\theta\theta}(r,t)=\sigma_{\mathrm{rock}}^{\phi\phi}(r,t)=2\frac{C(t)}{r^3}. \tag{A30}$$

The dimensionless boundary conditions corresponding to (A19a), (A19c), (A19e), and (A20) become

$$P_l(t)+\sigma_m^{\mathrm{rr}}\left(\frac{r_o}{R_o},t\right)=0 \tag{A31a}$$

$$P_f\left(\frac{r_o}{R_o},t\right)-P_l(t)=0 \tag{A31b}$$

$$\nabla P_f(1,t)=0 \tag{A31c}$$

$$-4u_m(1,t)-\sigma_m^{rr}(1,t)=0. \tag{A31d}$$

The dimensionless boundary condition (A31) states the constraints on the displacement, stresses, and pressures in the system, which can be transformed into constraints for the variation in fluid content $m(r,t)$. To do

so, we use the equilibrium solutions (A25)–(A28) to express the boundary values $P_f(\frac{r_o}{R_o},t)$, $u_m(\frac{r_o}{R_o},t)$, $\sigma_m^{rr}(\frac{r_o}{R_o},t)$ and $\sigma_m^{rr}(1,t)$ then substitute the inner boundary value $u_m(\frac{r_o}{R_o},t)$ into (A29) to obtain P_l:

$$P_f\left(\frac{r_o}{R_o},t\right)=a_1 m\left(\frac{r_o}{R_o},t\right)+a_2\zeta(t) \tag{A32a}$$

$$u_m\left(\frac{r_o}{R_o},t\right)=b_1\int_{\frac{r_o}{R_o}}^{1} r'^2 m(r',t)\mathrm{d}r'+b_2\zeta(t)+u_m(1,t)\frac{R_o^2}{r_o^2} \tag{A32b}$$

$$\sigma_m^{\mathrm{rr}}\left(\frac{r_o}{R_o},t\right)=c_1\int_{\frac{r_o}{R_o}}^{1} r'^2 m(r',t)\mathrm{d}r'+c_2\zeta(t)-4\frac{R_o^3}{r_o^3}\frac{\mu_m}{\mu_r}u_m(1,t) \tag{A32c}$$

$$\sigma_m^{\mathrm{rr}}(1,t)=\zeta(t)-4\frac{\mu_m}{\mu_r}u_m(1,t) \tag{A32d}$$

$$P_l(t)=d_1\int_{\frac{r_o}{R_o}}^{1} r^2 m(r,t)\mathrm{d}r+d_2\zeta(t)-\frac{3K_l R_o^3}{\mu_r r_o^3}u_m(1,t)+\begin{cases}\frac{K_l}{\mu_r}\frac{\Delta M}{M_o t_{\mathrm{inj}}}\left(t-(t-t_{\mathrm{inj}})H(t-t_{\mathrm{inj}})\right)\\ \frac{K_l}{\mu_r}\frac{\Delta M}{M_o}\end{cases}, \tag{A32e}$$

where the lower case in (A32e) corresponds to the end member of a sudden injection and the constant values $a_1, a_2, b_1, b_2, c_1, c_2, d_1$, and d_2 are determined by the mechanical properties of the system:

$$a_1=\frac{(K_m+\frac{4}{3}\mu_m)(K_u-K_m)}{\alpha^2\mu_r(K_u+\frac{4}{3}\mu_m)},\qquad a_2=-\frac{K_u-K_m}{\alpha(K_u+\frac{4}{3}\mu_m)}$$

$$b1=-\frac{R_o^2}{r_o^2}\frac{K_u-K_m^3}{\alpha(K_u+\frac{4}{3}\mu_m)},\qquad b_2=-\frac{\mu_r}{K_u+\frac{4}{3}\mu_m}\frac{1}{3}\left(\frac{R_o^2}{r_o^2}-\frac{r_o}{R_o}\right)$$

$$c_1=\frac{4R_o^3}{r_o^3}\frac{\mu_m}{\mu_r}\frac{K_u-K_m}{\alpha(K_u+\frac{4}{3}\mu_m)},\qquad c_2=1+\frac{4\mu_m}{K_u+\frac{4}{3}\mu_m}\frac{1}{3}\left(\frac{R_o^3}{r_o^3}-1\right)$$

$$d_1=-\frac{3K_l R_o^3}{\mu_r r_o^3}-b_1\frac{3K_l R_o}{\mu_r r_o},\qquad d_2=-b_2\frac{3K_l R_o}{\mu_r r_o}.$$

Substituting (A32d) into the boundary condition (A31d), we obtain the relation between $u_m(1,t)$ and $\zeta(t)$:

$$\zeta(t)=e_o u_m(1,t),\qquad e_o=4\left(\frac{\mu_m}{\mu_r}-1\right) \tag{A33}$$

which, together with (A32e), (A32a), and (A32c), transform the boundary conditions (A31a)–(A31c) to

$$f_1 m\left(\frac{r_o}{R_o},t\right)+f_2 u_m(1,t)+f_3\int_{\frac{r_o}{R_o}}^{1} m(r',t)r'^2\mathrm{d}r-f_4=0 \tag{A34a}$$

$$g_1\int_{\frac{r_o}{R_o}}^{1} m(r',t)r'^2\mathrm{d}r'+g_2 u_m(1,t)+f_4=0 \tag{A34b}$$

$$\frac{\partial m}{\partial r}(1,t)=0, \tag{A34c}$$

where the dimensionless constants

$$f_1=a_1,\quad f_2=(a_2-d_2)e_o+\frac{3K_l}{\mu_r}\frac{R_o^3}{r_o^3},\quad f_3=-d_1$$

$$f_4=\begin{cases}\frac{K_l}{\mu_r}\frac{\Delta M}{M_o t_{\mathrm{inj}}}\left(t-(t-t_{\mathrm{inj}})H(t-t_{\mathrm{inj}})\right), & \text{gradual injection} t_{\mathrm{inj}}>0\\ \frac{K_l}{\mu_r}\frac{\Delta M}{M_o}, & \text{sudden injection} t_{\mathrm{inj}}\to 0\end{cases}$$

$$g_1=c_1+d_1,\qquad g_2=(c_2+d_2)e_o-\frac{R_o^3}{r_o^3}\left(4\frac{\mu_m}{\mu_r}+3\frac{K_l}{\mu_r}\right)$$

Eliminating $u_m(1,t)$, (A34) finally leads to the constrains on m on the boundaries

$$f_1 m\left(\frac{r_o}{R_o},t\right)+\left(f_3-\frac{f_2 g_1}{g_2}\right)\int_{\frac{r_o}{R_o}}^{1} m(r,t)r^2\mathrm{d}r-\left(f_4+\frac{f_2 f_4}{g_2}\right)=0 \tag{A35a}$$

$$\frac{\partial m}{\partial r}(1,t)=0. \tag{A35b}$$

The initial condition for m is

$$m(r,0)=0,\qquad \left(\frac{r_o}{R_o}<r<1\right), \tag{A36}$$

indicating that initially, magma is not moving in the shell. The solution for $m(r,t)$ is uniquely determined by the boundary and initial conditions (A35) and (A36), which can lead to the solution $u_m(1,t)$ and $\zeta(t)$ using (A34) and (A33). The solutions for other quantities can be further obtained using (A25)–(A28).

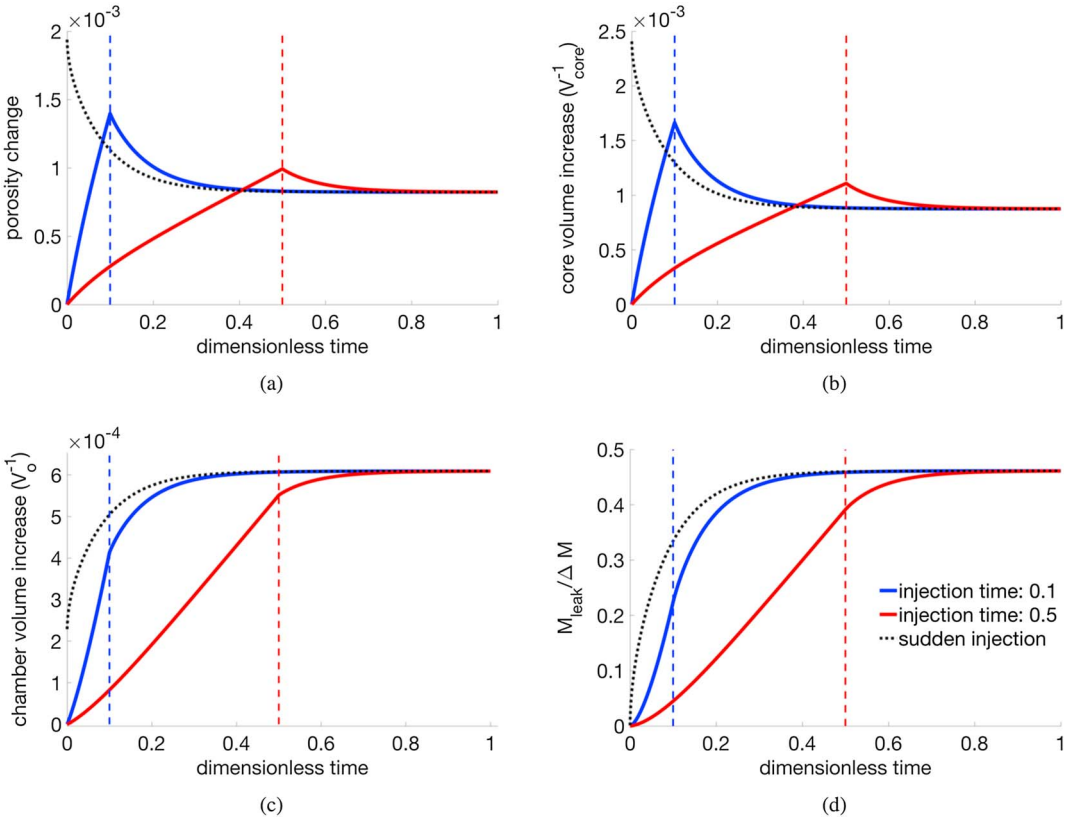

Figure A1. Evolution of (a) porosity change at the core-mush boundary, (b) relative increase in liquid core volume, (c) relative increase in total chamber volume, and (d) mass of magma leaked from the liquid core into the shell, as functions of time, following injection with normalized injection time period of 0.1 (blue) and 0.5(red), respectively. Blue and red dashed lines indicate the moments when the injection terminates. When the injection period is infinitely short in the case of an instantaneous injection, the evolutions are shown in black dotted line. The system has the same parameters with Figure 4 in the main text.

A2.6. Numerical Solution for the Evolution of the System on Gradual Injection

As shown above, the evolutions of the displacement and stresses in the system can be obtained by solving the governing equation:

$$\frac{\partial}{\partial t}m(r,t) - \nabla^2 m(r,t) = 0 \tag{A37}$$

in spherical coordinates, with the initial and boundary conditions

$$f_1 m\left(\frac{r_o}{R_o}, t\right) + h_0 \int_{\frac{r_o}{R_o}}^{1} m(r',t) r'^2 \mathrm{d}r = h_1 \tag{A38a}$$

$$\frac{\partial m}{\partial r}(1,t) = 0 \tag{A38b}$$

$$m(r,0) = 0, \qquad \left(\frac{r_o}{R_o} < r < 1\right), \tag{A38c}$$

where the constants

$$h_0 = f_3 - \frac{f_2 g_1}{g_2}, \qquad h_1 = f_4 + \frac{f_2 f_4}{g_2}$$

are determined by the micromechanical properties and geometry of the system (f_1, f_2, f_3, f_4, g_1, and g_2 are defined in Appendix A2.5).

The system determined by (A37) and (A38) can be solved either numerically or analytically. For numerical solution, we employ a finite difference scheme. At each time step, m is integrated across the mush shell to obtain the boundary value for the following time step. We use the numerical solution for the case of gradual injection

over finite period of injection time ($t_{inj} > 0$) and find that the system keeps evolving after the injection terminates (when $t > t_{inj}$). During gradual injection, the syninjection increase of the core pressure is accompanied by the expansion of the fluid core volume (see Figures 4, A1a, and A1c). The maximum core pressure and core volume are achieved at the end of the injection, and their values increase with more rapid injection. After the injection terminates, the core pressure and volume decrease, due to the continuous leading of magma into the mush shell (see Figure A1d).

Once the fluid content $m(r, t)$ is fully solved, we use the relations in (A34a) and A33 to obtain $u_m(1, t)$ and $\zeta(t)$:

$$u_m(1,t) = -\frac{f_1}{f_2} m\left(\frac{r_o}{R_o}, t\right) - \frac{f_3}{f_2}\int_{\frac{r_o}{R_o}}^{1} m(r',t) r'^2 \mathrm{d}r + \frac{f_4}{f_2}, \qquad \zeta(t) = e_0 u_m(1,t), \tag{A39}$$

which lead to solutions for the displacement and stress in the mush shell via (A26) and (A28). As magma flows from the liquid core into the mush shell, the volumes of the pore spaces and the total mush shell expand, leading to changes in the porosity $\Delta\phi = \Delta(V_{pore}/V_{total})$, where V_{pore} and V_{total} are the pore fluid volume filling up the deformed pore space and total volume of a deformed, infinitesimal small segment in the mush. Using chain rule, we evaluate the change in porosity by expanding the first-order changes with regard to the equilibrium state:

$$\begin{aligned}
\Delta\left(\frac{V_{pore}}{V_{total}}\right) &= \frac{\Delta V_{pore}}{V_{total,0}} - \frac{V_{pore,0}}{V_{total,0}}\frac{\Delta V_{total}}{V_{total,0}} \\
&= \frac{1}{V_{total,0}}\Delta\left(\frac{M_{fluid}}{\rho_f}\right) - \phi_0 \nabla\cdot\vec{u}_m \\
&= \frac{1}{V_{total,0}}\left(\frac{\Delta M_{fluid}}{\rho_{f,0}} - \frac{M_{fluid,0}}{\rho_{f,0}}\frac{\Delta\rho_f}{\rho_{f,0}}\right) - \phi_0\nabla\cdot\vec{u}_m \\
&= m(r,t) - \phi_0\left(\frac{\mu_r}{K_f}P_f(r,t) + \nabla\cdot\vec{u}_m(r,t)\right),
\end{aligned} \tag{A40}$$

where $m(r, t)$, $P_f(r, t)$, and $\vec{u}_m(r, t)$ are the dimensionless solutions obtained via the numerical solution, M_{fluid} denotes the mass of pore magma in the mush segment, and K_f is the bulk modulus of the pore magma. We use this relation to evaluate the change in porosity and find that the porosity changes is typically small, on the order of 10^{-3}.

Outside the chamber, the displacement and stress components can be obtained via the continuity of displacement on the mush-rock boundary: Using $u_{rock}(1, t) = u_m(1, t)$, the time-dependent function $C(t)$ in (A30) is thus determined $C(t) = u_m(1, t)$, leading to the displacement and the dimensionless stress components in the crust:

$$u_{rock}(r,t) = \frac{u_m(1,t)}{r^3}, \qquad \sigma^{rr}_{rock} = \frac{-4u_m(1,t)}{r^3}, \qquad \sigma^{\theta\theta}_{rock}(r,t) = \sigma^{\phi\phi}_{rock}(r,t) = \frac{2u_m(1,t)}{r^3}, \tag{A41}$$

which has a dependence on r similar to the solutions around an elastic inclusion (Landau & Lifshitz, 1959; Mogi, 1958).

We also notice that when the injection period decreases and the injection rate increases, the syninjection and postinjection evolution of the system approaches the end member case of a sudden injection (see both Figure A1 and Figure 4). Meanwhile, for the sudden injection, the system takes the longest time to approach its final steady state. We consider the time scale associated with the transient evolution following a sudden injection, which is independent of either the injected amount of magma or the injection rate, as an intrinsic time scale for the system. Below, we study this end member case in order to obtain its transient evolution, as well as the intrinsic time scale.

A2.7. Analytical Solution for Sudden Injection

In this section, we solve the governing equations (A37) and (A38) for the case of a sudden injection event, in order to obtain a postinjection time scale that is independent of the injection rate.

The evolution of the system during the diffusion of pore pressure and stress can be solved using Laplace transform. For a dimensionless function $f(r, t)$ (r and t are normalized with their respective scales), we denote

$$\bar{f}(r) = \mathcal{L}(f) = \int_0^\infty f(r,t)e^{-st}\mathrm{d}t \tag{A42}$$

where s is a complex variable. We can show straightforwardly that the Laplace transform of the new function $\partial f/\partial t$ becomes

$$\overline{\frac{\partial f}{\partial t}}(r) = s\bar{f}(r) - f(r,0), \tag{A43}$$

where $f(r,0)$ is the initial value of f at time $t = 0$. Once the solution for $\bar{f}(r,s)$ is obtained, $f(r,t)$ can be calculated using the inversion in complex space $f(r,t) = \int_{\sigma-i\infty}^{\sigma+i\infty} \bar{f}(r)e^{st}$s, where $\sigma > 0$ is a large positive value. We apply the Laplace transform for all terms on the evolution equations (A37) and (A38) and use the initial condition of m to obtain the governing equation for the Laplace transform of m:

$$\nabla^2\bar{m}(r) - s\bar{m}(r) = 0 \tag{A44a}$$

$$f_1\bar{m}\left(\frac{r_o}{R_o}\right) + h_o\int_{\frac{r_o}{R_o}}^{1}\bar{m}(r')r'^2\mathrm{d}r - \frac{h_1}{s} = 0 \tag{A44b}$$

$$\frac{\partial\bar{m}}{\partial r}(1) = 0, \tag{A44c}$$

which is a second-order ordinary differential equation fully determined by two boundary conditions. The radial symmetric solution for (A44a) in spherical coordinates has solutions with forms of spherical Bessel functions (with imaginary wavenumber of $\pm i\sqrt{s}$):

$$\bar{m}(s) = A\frac{e^{r\sqrt{s}}}{r} + B\frac{e^{-r\sqrt{s}}}{r}, \tag{A45}$$

where A and B are coefficients to be determined using the boundary conditions (A44b) and (A44c). Substituting (A45) into the boundary condition at the mush-rock interface (A44c), we obtain the relation

$$B = \lambda(s)A, \qquad \lambda(s) = \frac{\sqrt{s}e^{\sqrt{s}} - e^{\sqrt{s}}}{\sqrt{s}e^{-\sqrt{s}} + e^{-\sqrt{s}}}. \tag{A46}$$

To determine A, we integrate (A45) with (A46) to obtain

$$\int_{r_o/R_o}^{1}\bar{m}r'^2\mathrm{d}r' = \lambda A\frac{(\sqrt{s}\frac{r_o}{R_o}+1)e^{-\sqrt{s}\frac{r_o}{R_o}}}{s} - A\frac{(\sqrt{s}\frac{r_o}{R_o}-1)e^{\sqrt{s}\frac{r_o}{R_o}}}{s}, \tag{A47}$$

which can be substituted into boundary condition (A44b), finally leading to

$$A = \frac{h_1}{2}\frac{(\sqrt{s}+1)e^{-\sqrt{s}}}{g(s)}, \qquad B = \frac{h_1}{2}\frac{(\sqrt{s}-1)e^{\sqrt{s}}}{g(s)}, \tag{A48}$$

where

$$\begin{aligned} g(s) =& \sqrt{s}\left(\frac{f_1R_o}{r_o}s + h_0\left(1-\frac{r_o}{R_o}\right)\right)\cosh\left(\sqrt{s}\left(1-\frac{r_o}{R_o}\right)\right) \\ &+ \left(\left(h_0\frac{r_o}{R_o} - \frac{f_1R_o}{r_o}\right)s - h_0\right)\sinh\left(\sqrt{s}\left(1-\frac{r_o}{R_o}\right)\right). \end{aligned} \tag{A49}$$

Substituting (A48) into (A45) and (A47), we obtain the solution for the Laplace transform of m

$$\bar{m}(r) = \frac{h_1}{r}\frac{\sqrt{s}\cosh(\sqrt{s}(1-r)) - \sinh(\sqrt{s}(1-r))}{g(s)}. \tag{A50}$$

The amount of magma leaked into the mush shell is defined by (A4), which is expressed by the dimensionless fluid content as $\frac{M_{\mathrm{leak}}}{M_o} = 3\left(\frac{R_o^3}{r_o^3}\right)\int_{\frac{r_o}{R_o}}^{1} m(r',t)r'^2\mathrm{d}r'$ and has the Laplace transform using (A50)

$$\overline{\frac{M_{\mathrm{leak}}}{M_o}} = 3\left(\frac{R_o^3}{r_o^3}\right)\int_{\frac{r_o}{R_o}}^{1}\bar{m}(r')r'^2\mathrm{d}r' = 3\left(\frac{R_o^3}{r_o^3}\right)\frac{h_1}{s}\frac{f(s)}{g(s)}, \tag{A51}$$

where

$$f(s) = \left(s\frac{r_o}{R_o} - 1\right)\sinh\left(\sqrt{s}\left(1-\frac{r_o}{R_o}\right)\right) + \sqrt{s}\left(1-\frac{r_o}{R_o}\right)\cosh\left(\sqrt{s}\left(1-\frac{r_o}{R_o}\right)\right)$$

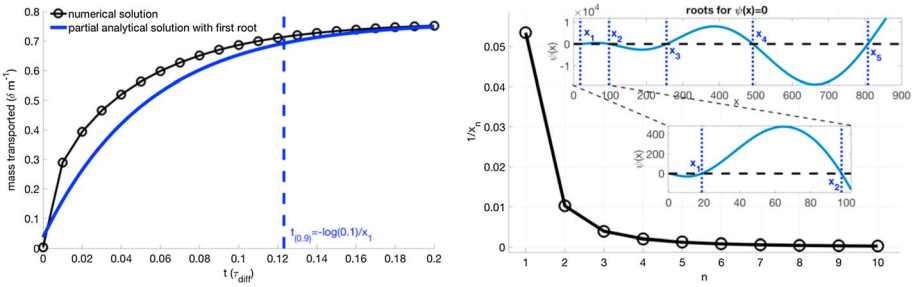

Figure A2. Decay time scales identified from the analytical solution. (a) Numerical solution for M_{leak}/M_o (black circle line) and analytical solution that only involves the decay functions up to $n = 1$. The dash line indicates the time corresponding to 90% decay, predicted from the slowest decay component. (b) Decay time scales $1/x$ corresponding to the first 10 roots $x_n \quad (n = 1 - 10)$ that satisfy the characteristic equation $\psi(x) = 0$ according to (A57), calculated for a system of $\phi_o = 0.2, R_o = 2r_o, K_l = K_f = 0.5\mu_r,\ \mu_m = 0.5\mu_r$, and $K_s = 5/3\mu_r$, and $\alpha = 0.9$. Insets show function $\psi(x)$ and x_n with increasing value. For the given parameters, the first positive root $x_1 = 18.69$, which yield a dimensionless decay time $1/x_1 = 0.053$.

Using the solutions (A50) and (A51), the solutions for $m(r, t)$ and $M_{\text{leak}}(t)$ in real time can be obtained by

$$m(r,t) = \frac{h_1}{r}\int_{\sigma-i\omega}^{\sigma+i\omega} \frac{\sqrt{s}\cosh(\sqrt{s}(1-r)) - \sinh(\sqrt{s}(1-r))}{g(s)} e^{st} ds \tag{A52a}$$

$$\frac{M_{\text{leak}}(t)}{M_o} = 3\frac{R_o^3}{r_o^3}\int_{\sigma-i\omega}^{\sigma+i\omega} \frac{h_1}{s}\frac{f(s)}{g(s)} e^{st} ds. \tag{A52b}$$

The integrations in (A52) can be calculated using the residual theorem. Without loss of generality, we demonstrate how to integrate (A52b). We identify the poles for the integrated function $\frac{h_1}{s}\frac{f(s)}{g(s)}e^{st}$ (in this case, the poles are zeros for the function $g(s)$, which render the integrated function meaningless) as s_n $(n = 0, 1, 2, ...)$. The integration is obtained by summing up the residuals at all poles:

$$\frac{M_{\text{leak}}(t)}{M_o} = 2\pi i \frac{3R_o^3}{r_o^3}\sum_n Res(s_n) \tag{A53}$$

in which the residual for the nth pole $Res(s_n)$ can be calculated according to the residual theorem:

$$Res(s_n) = \frac{1}{2\pi i}\lim_{s\to s_n}(s - s_n)\frac{h_1}{s}\frac{f(s)}{g(s)}e^{st} \tag{A54}$$

We calculate the limit in (A54) using the L'hopital's law and obtain

$$Res(s_n) = \frac{1}{2\pi i}\frac{h_1}{s_n}\frac{f(s_n)}{g'(s_n)}e^{s_n t} = -\frac{h_1 e^{-x_n t}}{2\pi i}\frac{f_1(x_n+1)}{E(x_n)}, \quad (n>0) \tag{A55a}$$

$$Res(s_0) = \frac{1}{2\pi i}h_1\frac{f''(s_0)}{g''(s_0)} \qquad = \frac{1}{2\pi i}h_1\frac{1-\frac{r_o^3}{R_o^3}}{3f_1 + h_o\left(1-\frac{r_o^3}{R_o^3}\right)}, \quad (n=0), \tag{A55b}$$

where g', g'', and f'' indicate the first derivative of $g(s)$, the second derivative of $g(s)$, and the second derivative of $f(s)$, respectively, evaluated at the poles. When $n = 0$, $s_0 = 0$, and when $n > 0$, we express the residuals with the inverse of the poles $x_n = -s_n$ and only allow $x_n > 0$, considering finite solutions with $e^{-x_n t} \to 0|_{t\to 0}$. The coefficient $E(x_n)$ in (A55a) is

$$E(x_n) = \frac{f_1^2\left(1-\frac{r_o}{R_o}\right)x_n^2}{2\frac{r_o^2}{R_o^2}} - \frac{2h_0f_1 - 3h_0f_1\frac{r_o}{R_o} + f_1^2 + h_0\frac{r_o^3}{R_o^3}\left(\frac{r_o}{R_o}-1\right)}{2\frac{r_o}{R_o}}x_n + \frac{h_0^2\left(1-\frac{r_o^3}{R_o^3}\right)}{2} + \frac{3}{2}h_0f_1 \tag{A56}$$

, and x_n are the positive solutions for $\psi(x) = 0$ (see Figure A2b inset panel), where the function $\psi(x) = ig(-x)$ is

$$\psi(x) = \left(\left(\frac{h_o r_o}{R_o} - \frac{f_1 R_o}{r_o}\right)x + h_0\right)\sin\left(\sqrt{x}\left(1 - \frac{r_o}{R_o}\right)\right) - \sqrt{x}\left(h_0\left(1 - \frac{r_o}{R_o}\right) - \frac{f_1 R_o x}{r_o}\right)\cos\left(\sqrt{x}\left(1 - \frac{r_o}{R_o}\right)\right). \tag{A57}$$

Substituting (A55) into (A53), we obtain the solution for the mass of magma transported to/from the shell $M_{\text{leak}}(t)$ as a function of time

$$\frac{M_{\text{leak}}(t)}{M_o} = 3\frac{R_o^3}{r_o^3}h_1\left(\frac{1 - \frac{r_o^3}{R_o^3}}{3f_1 + h_o\left(1 - \frac{r_o^3}{R_o^3}\right)} - f_1\sum_{n=1}^{\infty}\frac{x_n + 1}{E(x_n)}e^{-x_n t}\right), \tag{A58}$$

where x_n and $E(x_n)$ are defined in (A57) and (A56). Following similar approach, the solution for $m(r, t)$ can be obtained by inverting (A50), which yields

$$m(r,t) = \frac{3h_1}{h_o\left(1 - \frac{r_o^3}{R_o^3}\right) + 3f_1} + \frac{h_1}{r}\sum_{n=1}^{\infty}\frac{h_o + x_n\left(\frac{h_o r_o}{R_o} - \frac{f_1 R_o}{r_o}\right)}{E(x_n)}G(x_n, r)e^{-x_n t} \tag{A59}$$

where

$$G(x_n, r) = \frac{\cos\left(\sqrt{x_n}(1 - r)\right)}{\cos\left(\sqrt{x_n}\left(1 - \frac{r_o}{R_o}\right)\right)}\left(1 - \frac{\tan\left(\sqrt{x_n}(1 - r)\right)}{\sqrt{x_n}}\right). \tag{A60}$$

Following the same steps in Appendix A2.6, $m(r, t)$ leads to the solutions for $u_m(1, t)$ and $\zeta(t)$ according to (A39), the displacement and radial stress in the mush via (A26) and (A28), and the displacement and stress components in the crust rocks via (A41).

A2.8. Time Scale of Postinjection Evolution

The solutions (A58) and (A59) consist of an infinite number of decay functions, each corresponding to a dimensionless decay rate x_n and decay time scale of $1/x_n$ $(n > 0)$. Because x_n increases with n, the slowest decay function has the minimum decay rate when $n = 1$ and the longest decay time scale $1/x_1$ (see Figure A2b). The longest decay time scale $1/x_1$ determines the long-term evolution of the solutions, while the other decay functions quickly damp out with time. This can be justified by comparing the full numerical solution and the analytical solution approximated using only the slowest decay function and the constant term (see Figure A2a). Comparing the numerical solution and the analytical solution based on the slowest decay term, we define the longest decay time $1/x_1$ as the dimensionless time scale for postinjection evolution. We note that the solution for x_1 strictly applies to the case of an instantaneous injection and marks the upper limit of the transient, postinjection time scale. Because $1/x_1$ is dimensionless, the actual time scale, denoted by t_{post}, is obtained by

$$t_{\text{post}} = \frac{1}{x_1}t^*, \tag{A61}$$

where $t^* = R_o^2/c$ is the system's time scale determined by the radius of the magma chamber and the poroelastic diffusivity c:

$$c = \frac{\kappa}{\eta_f}\frac{(K_m + \frac{4}{3}\mu_m)(K_u - K_m)}{\alpha^2(K_u + \frac{4}{3}\mu_m)}. \tag{A62}$$

Substituting the expression for c into t^*, we obtain the postinjection dimensional time scale t_{post}

$$t_{\text{post}} = \left(\frac{R_o^2\eta_f}{\kappa\mu_r}\right)\left(\frac{1}{x_1}\frac{\alpha^2\left(\frac{K_u}{\mu_r} + \frac{4}{3}\frac{\mu_m}{\mu_r}\right)}{\left(\frac{K_m}{\mu_r} + \frac{4}{3}\frac{\mu_m}{\mu_r}\right)\left(\frac{K_u}{\mu_r} - \frac{K_m}{\mu_r}\right)}\right) = t_{\text{system}}\tau_m, \tag{A63}$$

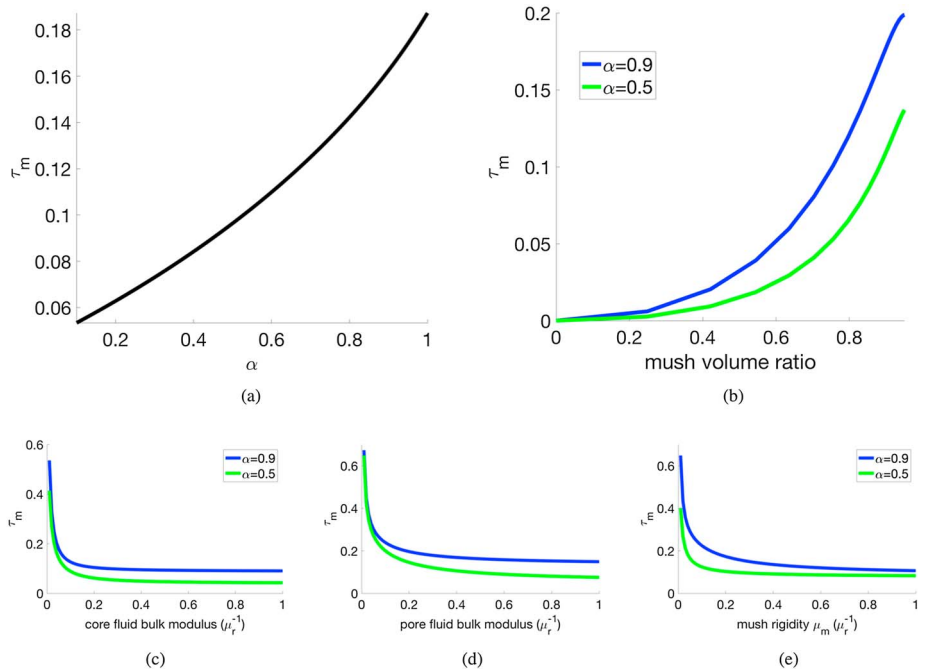

Figure A3. The mush-dependent time coefficient τ_m as functions of mush and fluid properties, according to (A64). The system has $\phi_o = 0.2$, for all panels. Panel (a) has $K_l = 0.1\mu_r$, $K_f = 0.5\mu_r$, $\mu_m = 0.5\mu_r$, $K_s = 5/3\mu_r$, and $R_o = 2r_o$; panel (b) has $K_l = 0.1\mu_r, K_f = 0.5\mu_r, \mu_m = 0.5\mu_r$, $K_s = 5/3\mu_r$, and $\alpha = 0.9$ or 0.5; panel (c) has $K_f = 0.5\mu_r$, $\mu_m = 0.5\mu_r, K_s = 5/3\mu_r, R_o = 2r_o$, and $\alpha = 0.9$ or 0.5; panel (d) has $K_l = 0.5\mu_r, \mu_m = 0.5\mu_r, K_s = 5/3\mu_r, R_o = 2r_o$, and $\alpha = 0.9$ or 0.5; panel (e) has $K_l = 0.5\mu_r, K_f = 0.5\mu_r, K_s = 5/3\mu_r, R_o = 2r_o$, and $\alpha = 0.9$ or 0.5.

which can be split into two terms: the term with the unit of time $t_{\text{system}} = \frac{R_o^2\eta_f}{\kappa\mu_r}$ depends on the physical dimension R_o, magma viscosity η_f, mush permeability κ, and rigidity of host rock μ_r. The dimensionless term τ_m only depends on the ratios between the quantities, as well as the solution for the dimensionless time scale $1/x_1$:

$$\tau_m\left(\frac{r_o}{R_o}, \alpha, \frac{\mu_m}{\mu_r}, \frac{K_m}{\mu_r}, \frac{K_u}{\mu_r}\right) = \frac{1}{x_1}\frac{\alpha^2\left(\frac{K_u}{\mu_r} + \frac{4}{3}\frac{\mu_m}{\mu_r}\right)}{\left(\frac{K_m}{\mu_r} + \frac{4}{3}\frac{\mu_m}{\mu_r}\right)\left(\frac{K_u}{\mu_r} - \frac{K_m}{\mu_r}\right)} \tag{A64}$$

in which x_1 is identified as the first positive root for the function $\psi(x, \frac{r_o}{R_o}, \alpha, \frac{\mu_m}{\mu_r}, \frac{K_m}{\mu_r}, \frac{K_u}{\mu_r}) = 0$. We find that τ_m varies most strongly with the relative structural strength in the mush (i.e., with poroelastic coefficient α), as well as the volume fraction of mush in the chamber (see Figures A3a and A3b). Apart from these two properties (which cause variations up to 2 orders of magnitudes), other micromechanical quantities, including the relative compressibility of either the core or the pore fluid and the relative rigidity of the mush, influence the value of τ_m to a smaller degree (up to 1 order of magnitude, see Figures A3c–A3e). In contrast, the system time scale t_{post} can cause discrepancies of many orders of magnitude, primarily due to the large uncertainties in the magma viscosity and the permeability of mush, as shown in the main text (Figure 5).

A2.9. Initial Response and Final Steady State Following a Sudden Injection

When the injection is infinitely rapid, the magma chamber responds to the initial sudden change in core pressure elastically. At the moment of the sudden injection, there is not enough time for the magma residing in the pore spaces to be transported. The mush therefore is in an undrained condition, with zero variation in the fluid content $m = 0$ everywhere, except for the liquid-mush boundary. Substituting the integration $\int_{\frac{r_o}{R_o}}^{1} r^2 m dm = 0$ into the boundary condition (A34), we can obtain the instantaneous displacement deformation of the chamber $u_m(1, 0^+)$ as well as the instantaneous increase in fluid content at the mush magma boundary $m\left(\frac{r_o}{R_o}, 0^+\right)$:

$$u_m(1, 0^+) = -\frac{f_4}{g_2}, \qquad m\left(\frac{r_o}{R_o}, 0^+\right) = \frac{f_4}{f_1} + \frac{f_2 f_4}{f_1 g_2}$$

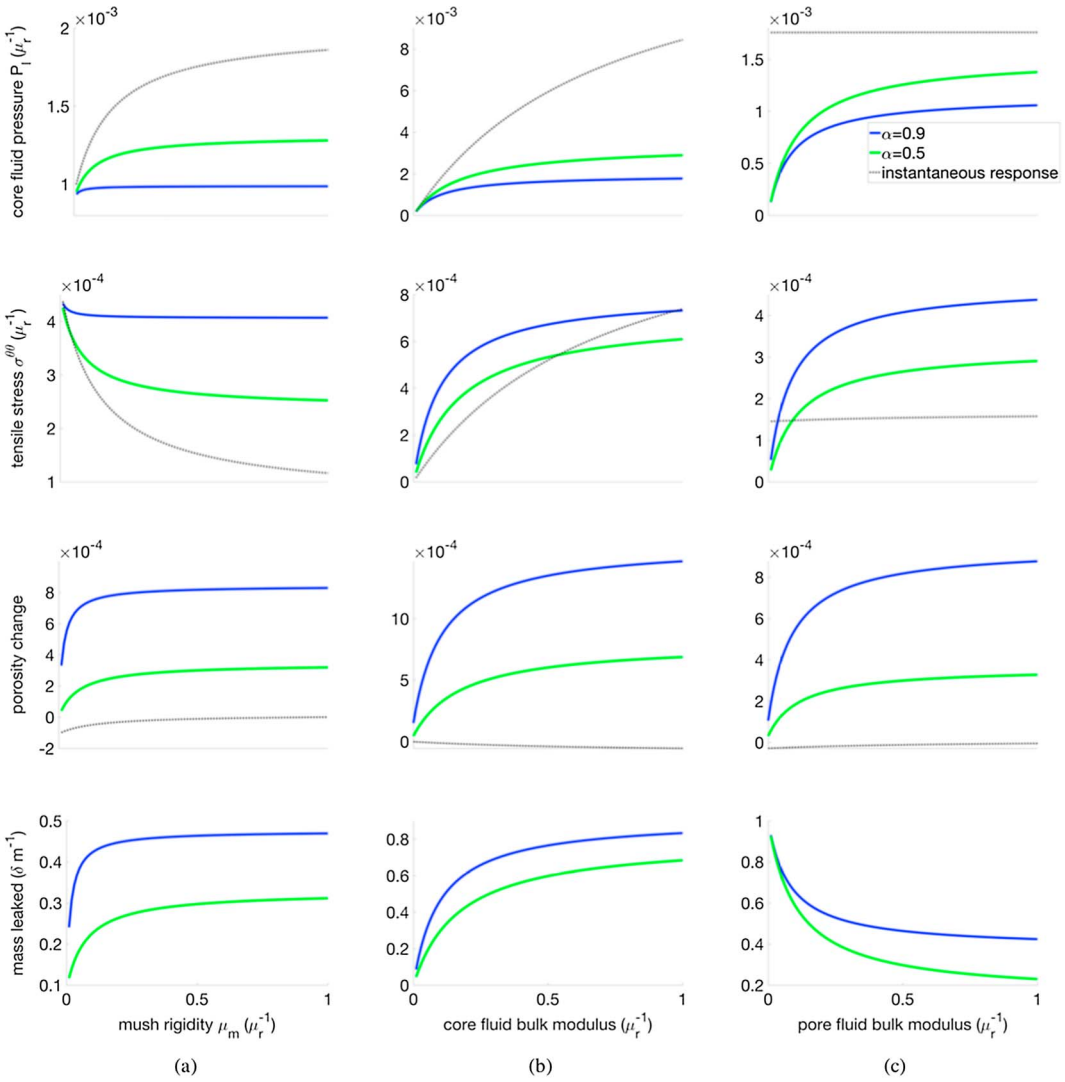

Figure A4. Initial response and final responses for a system with parameters $\phi_o = 0.2, K_l = 0.1\mu_r, K_f = 0.5\mu_m$, $\mu_m = 0.5\mu_r$, and $K_s = 5/3\mu_r$. Column (a) shows variations in mush rigidity μ_m, column (b) shows variations in the bulk modulus of the core fluid K_l, and column (c) shows variations in the bulk modulus of the pore fluid K_f. The changes in the mush final states are calculated for both $\alpha = 0.5$ (green) and $\alpha = 0.9$ (blue). For both α values, the initial responses are similar, hence shown by one curve (black dash line). The injected mass is $\Delta M = 2\% M_o$.

, which is substituted into (A32) and (A34) to obtain the instantaneous response in core pressure $P_l(0^+)$. Using (A30c) and (A19e), the tensile stress in the rocks $\sigma^{\theta}_{\text{rock}}\theta(1, 0^+) = 2u_m(1, 0^+)$ can be obtained:

$$P_l(0^+) = \left(1 - \frac{e_0 d_2}{g_2} + \frac{3K_l}{g_2\mu_r}\frac{R_o^3}{r_o^3}\right)\frac{K_l}{\mu_r}\frac{\Delta M}{M_o}, \qquad \sigma^{\theta\theta}_{\text{rock}}(1, 0^+) = -\frac{2}{g_2}\frac{K_l}{\mu_r}\frac{\Delta M}{M_o}.$$

The instantaneous response of the system upon a sudden injection is equivalently an elastic response, wherein the effective bulk modulus is the undrained modulus K_u. It is worth noting that the instantaneous response calculated above would be the same response if the mush shell is impermeable (e.g., if the porosity in the mush is not high enough to reach the percolation threshold), or if the diffusion of pore magma is too slow compared to the injection. In this case, the instantaneous response will persist in time. In the last section, we will use this end member case to obtain a solution for viscoelastic deformation in the mush shell.

Long after the injection, the system approaches a new steady state, whose characteristics can be obtained straightforwardly from the analytical solution. Let $t \to \infty$, the time-dependent decay components in the

solutions (A58) and (A59) vanish, and only the time-independent components are left:

$$m(r,\infty)=\frac{3\left(1+\frac{f_2}{g_2}\right)}{h_o\left(1-\frac{r_o^3}{R_o^3}\right)+3f_1}\frac{K_l}{\mu_r}\frac{\Delta M}{M_o},\qquad \frac{M_{\text{leak}}(\infty)}{M_o}=\frac{3\left(1+\frac{f_2}{g_2}\right)\left(\frac{R_o^3}{r_o^3}-1\right)}{3f_1+h_o(1-\frac{r_o^3}{R_o^3})}.$$

At the steady state, the fluid content m at the core-mush boundary $m\left(\frac{r_o}{R_o},\infty\right)$ is the same as the interior of the mush, which can be substituted into the boundary condition (A34), (A33), and the relations in (A32) to obtain the steady state response in other quantities, including the core pressure and the tensile stress:

$$P_l(\infty)=\frac{K_l}{\mu_r}\frac{\Delta M}{M_o}\left(1+\frac{1}{g_1}\left(\frac{3K_l}{\mu_r}\frac{R_o^3}{r_o^3}-d_2e_o\right)+\frac{\left(1+\frac{f_2}{g_2}\right)\left(1-\frac{r_o^3}{R_o^3}\right)}{3f_1+h_o\left(1-\frac{r_o^3}{R_o^3}\right)}\left(d_1+\frac{g_1}{g_2}\left(\frac{3K_l}{\mu_r}\frac{R_o^3}{r_o^3}-d_2e_o\right)\right)\right)$$

$$\sigma_{\text{rock}}^{\theta\theta}(1,\infty)=2u_m(1,\infty)=-\frac{2K_l}{g_2\mu_r}\frac{\Delta M}{M_o}\left(1+\frac{g_1\left(1-\frac{r_o^3}{R_o^3}\right)\left(1+\frac{f_2}{g_2}\right)}{3f_1+h_o\left(1-\frac{r_o^3}{R_o^3}\right)}\right).$$

We find that among the micromechanical properties, α and the mush content have the most prominent influence on the final steady state of the system (Figure 6 in the main text). Other quantities, such as the rigidity of the mush and the compressibility of the magma in the core or pore space, play lesser roles in determining the steady state (see Figure A4).

A3. Postinjection Evolution for an Effectively Viscoelastic Mush Shell

To probe the similarity and differences between the two rheologies of poroelasticity and viscoelasticity, we assume that the crystalline matrix in the mush shell behaves as a Maxwell linear solid. By assuming that the pore magma is trapped in the pore space (i.e., undrained condition), the mush shell behaves as a viscoelastic material effectively. Similar to the standard practice of calculating the transient evolution for viscoelastic material using Laplace transform on the solution for elastic deformation, here we use the solution obtained for the instantaneous poroelastic response upon a sudden injection (i.e., with undrained condition) to obtain the viscoelastic solution. We first calculate the Laplace-transformed solution for the poroelastic shell under the undrained condition. By applying Laplace transform on the boundary condition (A34b), substituting the undrained condition for $m(r,t)=0$ and assuming a Maxwell viscoelasticity that effects only the shear bulk modulus μ_m, we obtain the Laplace transform for the radial displacement $u_m(1,t)$ at the mush-rock interface:

$$\overline{u_m(1)}=-\frac{\widetilde{f_4}}{\widetilde{g_2}},\tag{A65}$$

where

$$\widetilde{g_2}=\frac{1}{K_u+\frac{4}{3}\tilde{\mu_m}}\left(\left(\frac{4}{\mu_r}\left(K_u-K_l-K_u\frac{R_o^3}{r_o^3}\right)-\frac{16}{3}\frac{R_o^3}{r_o^3}\right)\tilde{\mu_m}-4\left(K_u+K_l\left(\frac{R_o^3}{r_o^3}-1\right)\right)-3\frac{K_lK_u}{\mu_r}\frac{R_o^3}{r_o^3}\right)$$

results from substituting the instantaneous shear modulus μ_m^o (we now use ^{o} to denote that the value corresponds to the poroelastic mush property) by the transformed time-dependent shear modulus for a Maxwell solid:

$$\tilde{\mu_m}\equiv\frac{\mu_m^o\eta_m s}{\eta_m s+\mu_m^o},$$

where η_m is the viscosity of the mush ensemble and s is the complex variable in the Laplace transform. The transform

$$\widetilde{f_4}=\frac{K_l\delta m}{\mu_r}\frac{1}{s}$$

results from the Laplace transform of the constant on the right-hand side of (A34b). Substituting the above expressions into (A65), we obtain the Laplace transform of the displacement at the mush-rock interface:

$$\overline{u_m}(1)=-\frac{K_l\delta m}{\mu_r}\frac{1}{s-s_{(0)}}\frac{\frac{K_u+\frac{4}{3}\mu_m^o}{l_0\mu_m^o-l_1}s+\frac{K_u\mu_m^o}{(l_0\mu_m^o-l_1)\eta_m}}{s-s_{(1)}},\tag{A66}$$

where the constants

$$I_0 = \frac{4}{\mu_r}\left(K_u - K_l - K_u\frac{R_o^3}{r_o^3}\right) - \frac{16}{3}\frac{R_o^3}{r_o^3}, \quad I_1 = 4\left(K_u + K_l\left(\frac{R_o^3}{r_o^3} - 1\right)\right) + 3\frac{K_l K_u}{\mu_r}\frac{R_o^3}{r_o^3}$$

The poles of $\overline{u_m(1)}$ are $s_{(0)}$ and $s_{(1)}$

$$s_{(0)} = 0, \qquad s_{(1)} = \frac{I_1\mu_m}{(I_0\mu_m^o - I_1)\eta_m} < 0$$

Substituting the solution (A66) into the Laplace-transformed boundary conditions (A33) and (A34), we obtain the Laplace transforms for other quantities, including the radial displacement at the fluid-mush boundary and the core pressure:

$$\overline{u_m}\left(\frac{r_o}{R_o}, s\right) = \frac{4}{3}\frac{K_l\delta m}{\mu_r}\left(\frac{R_o^2}{r_o^2} - \frac{r_o}{R_o}\right)\tilde{\Phi}(s) + \frac{R_o^2}{r_o^2}\overline{u_m}(1) \tag{A67a}$$

$$\overline{P_l}(s) = -\frac{4K_l^2\delta m}{\mu_r^2}\left(\frac{R_o^3}{r_o^3} - 1\right)\tilde{\Phi}(s) - \frac{3K_l}{\mu_r}\frac{R_o^3}{r_o^3}\overline{u_m}(1) + \frac{K_l\delta_m}{\mu_r}\frac{1}{s}, \tag{A67b}$$

where $\tilde{\Phi}(s)$ is an s-dependent function

$$\tilde{\Phi}(s) \equiv \frac{\mu_m^o - \mu_r}{I_0\mu_m^o - I_1}\frac{1}{s - s_{(0)}}\frac{s - \frac{\mu_r}{\mu_m^o - \mu_r}\frac{\mu_m^o}{\eta_m}}{s - s_{(1)}} \tag{A68}$$

Following similar approach in Appendix A2.7, we transform (A66) to obtain the solution for $u_m(1,t)$ in real time:

$$u_m(1,t) = \int_{\sigma-i\infty}^{\sigma+i\infty}\overline{u_m(1)}e^{st}\mathrm{d}s = \lim_{s\to s_{(0)}}(s - s_{(0)})\overline{u_m(1)}e^{st} + \lim_{s\to s_{(1)}}(s - s_{(1)})\overline{u_m(1)}e^{st}. \tag{A69}$$

Note that for this case, we do not normalize the time in the system (because the viscoelastic relaxation and the poroelastic time scale are independent), and therefore, the poles $s_{(0)}$ and $s_{(1)}$ have unit of frequency, and t has the unit of time. Substituting (A66) into the (A69), we obtain the solution in real time

$$u_m(1,t) = \frac{K_u K_l\delta m}{\mu_r I_1} - \frac{K_l\delta m}{\mu_r}\left(\frac{K_u + \frac{4}{3}\mu_m^o}{I_0\mu_m^o - I_1} + \frac{K_u}{I_1}\right)e^{s_{(1)}t}. \tag{A70}$$

Following similar approach, we transform (A67) to obtain

$$u_m\left(\frac{r_o}{R_o}, t\right) = \frac{4}{3}\frac{K_l\delta m}{\mu_r}\left(\frac{R_o^2}{r_o^2} - \frac{r_o}{R_o}\right)\Phi(t) + \frac{R_o^2}{r_o^2}u_m(1,t) \tag{A71a}$$

$$P_l(t) = -\frac{4K_l^2\delta m}{\mu_r^2}\left(\frac{R_o^3}{r_o^3} - 1\right)\Phi(t) - \frac{3K_l}{\mu_r}\frac{R_o^3}{r_o^3}u_m(1,t) + \frac{K_l\delta_m}{\mu_r}, \tag{A71b}$$

where the time-dependent function

$$\Phi(t) = \mathcal{L}^{-1}(\Phi(s)) = \frac{\mu_r}{I_1} + \left(\frac{\mu_m^o - \mu_r}{I_0\mu_m^o - I_1} - \frac{\mu_r}{I_1}\right)e^{s_{(1)}t}. \tag{A72}$$

The displacement in the mush also leads to the evolution of the tensile stress (see Appendix A2.9), as well as the approximated relative increase of the volume of the liquid core

$$\sigma_{\mathrm{rock}}^{\theta\theta}(1,t) = 2u_m(1,t), \qquad \frac{\Delta V_{\mathrm{core}}(t)}{V_{\mathrm{core},(0)}} \sim \frac{4\pi r_o^2 u_m\left(\frac{r_o}{R_o}, t\right)R_o}{\frac{4}{3}\pi r_o^3} = 3u_m\left(\frac{r_o}{R_o}, t\right)\frac{R_o}{r_o}. \tag{A73}$$

The three quantities P_l, $\sigma^{\theta\theta}$, and $\frac{\Delta V_{\mathrm{core}}}{V_{\mathrm{core},(0)}}$ are then compared to those obtained using the poroelastic model, as shown in Figure 8. Similar to the case of a poroelastic mush shell, we can define a postinjection evolution time scale using the slowest decay component in the solutions for the viscoelastic shell. Because $s_{(1)}$ is always

negative, the quantities shown above consist of a constant value and a single decay function with decay rate $-s_{(1)}$ and decay time scale

$$t_{\text{post}}^{\text{visc}} = -1/s_{(1)} = \frac{\eta_m}{\mu_m^o}\left(1 - \frac{l_o \mu_m^o}{l_1}\right). \tag{A74}$$

We notice that $t_{\text{post}}^{\text{visc}}$ does not depend on the actual value of R_o. This is because that the viscoelastic time scale η_m/μ_m^o, which determines the actual time unit in $t_{\text{post}}^{\text{visc}}$ (i.e., it is the counterpart of t_{system} for the poroelastic case), is an intrinsic material property independent of the dimension of the system. In contrast, the postinjected evolution time for the poroelastic shell, defined in (A63), increases with the chamber's radius.

Acknowledgments
We thank James Rice, Tushar Mittal, Chris Huber and Helge Gonnerman for useful discussions in the early stages of this work. S. Adam Soule was supported by National Science Foundation Grant OCE-1333492. Meghan Jones was supported by the U.S. Department of Defense through the National Defense Science and Engineering Graduate Fellowship (NDSEG) Program. The numerical codes used for computing the results in the work can be found at https://github.com/YangVol/MushyChamber.

References

Aharonov, E., & Sparks, D. (1999). Rigidity phase transition in granular packings. *Physical Review E*, *60*, 6890–6896.
Amoruso, A., & Crescentini, L. (2009). Shape and volume change of pressurized ellipsoidal cavities from deformation and seismic data. *Journal of Geophysical Research*, *114*, B02210. https://doi.org/10.1029/2008JB005946
Anderson, A. T., Swihart, GH., Artioli, G., & Geiger, C. A. (1984). Segregation vesicles, gas filter-pressing, and igneous differentiation. *The Journal of Geology*, *92*, 55–72.
Bachmann, O., & Bergantz, GW. (2004). On the origin of crystal-poor rhyolites: Extracted from batholithic crystal mushes. *Journal of Petrology*, *45*, 1565–1582. https://doi.org/10.1093/petrology/egh019
Bachmann, O., & Bergantz, GW. (2006). Gas percolation in upper-crustal silicic crystal mushes as a mechanism for upward heat advection and rejuvenation of near-solidus magma bodies. *Journal of Volcanology and Geothermal Research*, *149*(1–2), 85–102. https://doi.org/10.1016/j.jvolgeores.2005.06.002
Bachmann, O., & Huber, C. (2016). Silicic magma reservoirs in the Earth's crust silicic magma reservoirs in the Earth's crust. *American Mineralogist*, *101*(11), 2377–2404. https://doi.org/10.2138/am-2016-5675
Barboni, M., Boehnke, P., Schmitt, A. K., Harrison, T. M., Shane, P., Bouvier, A. S., & Baumgartner, L. (2016). Warm storage for arc magmas. *Proceedings of the National Academy of Sciences*, *113*(49), 13,959–13,964.
Bergantz, G. W., Schleicher, J. M., & Burgisser, A. (2015). Open-system dynamics and mixing in magma mushes. *Nature Geosci*, *8*(10), 793–796. https://doi.org/10.1038/ngeo2534
Biot, MA. (1941). General theory of three-dimensional consolidation. *Journal of Applied Physics*, *12*, 155–164.
Blake, S. (1981). Volcanism and the dynamics of open magma chambers. *Nature*, *289*, 783–785. https://doi.org/10.1038/289783a0
Browning, J., Drymoni, K., & Gudmundsson, A. (2015). Forecasting magma-chamber rupture at Santorini Volcano, Greece. *Scientific Reports*, *5*, 15785. https://doi.org/10.1038/srep15785
Caricchi, L., & Blundy, J. (2015). The temporal evolution of chemical and physical properties of magmatic systems. *Geological Society, London, Special Publications*, *422*(1), 1–15. https://doi.org/10.1144/SP422.11
Cashman, K. V., Sparks, R. S. J., & Blundy, J. D (2017). Vertically extensive and unstable magmatic systems: A unified view of igneous processes. *Science*, *355*(6331), eaag3055. https://doi.org/10.1126/science.aag3055
Cheng, A. H. D. (2016). *Poroelasticity*. AG, Switzerland: Springer International Publishing. https://doi.org/10.1007/978-3-319-25202-5
Chouet, B., Dawson, P., & Nakano, M. (2006). Dynamics of diffusive bubble growth and pressure recovery in a bubbly rhyolitic melt embedded in an elastic solid. *Journal of Geophysical Research*, *111*, B07310. https://doi.org/10.1029/2005JB004174
Costa, A. (2005). Viscosity of high crystal content melts: Dependence on solid fraction. *Geophysical Research Letters*, *32*, L22308. https://doi.org/10.1029/2005GL024303
Costa, A., Caricchi, L., & Bagdassarov, N. (2009). A model for the rheology of particle-bearing suspensions and partially molten rocks. *Geochemistry, Geophysics, Geosystems*, *10*, Q03010. https://doi.org/10.1029/2008GC002138
Crisp, J. A. (1984). Rates of magma emplacement and volcanic output. *Journal of Volcanology and Geothermal Research*, *20*(3), 177–211. https://doi.org/10.1016/0377-0273(84)90039-8
Davis, P. M. (1986). Surface deformation due to inflation of an arbitrarily oriented triaxial ellipsoidal cavity in an elastic half-space, with reference to Kilauea volcano, Hawaii. *Journal of Geophysical Research*, *91*(B7), 7429–7438. https://doi.org/10.1029/JB091iB07p07429
Degruyter, W., & Huber, C. (2014). A model for eruption frequency of upper crustal silicic magma chambers. *Earth and Planetary Science Letters*, *403*, 117–130. https://doi.org/10.1016/j.epsl.2014.06.047
Dragoni, M., & Magnanensi, C. (1989). Displacement and stress produced by a pressurized, spherical magma chamber, surrounded by a viscoelastic shell. *Physics of the Earth and Planetary Interiors*, *56*(3), 316–328. https://doi.org/10.1016/0031-9201(89)90166-0
Dzurisin, D. (2003). A comprehensive approach to monitoring volcano deformation as a window on the eruption cycle. *Reviews of Geophysics*, *41*(1), 1001. https://doi.org/10.1029/2001RG000107
Gelman, S. E., Gutiérrez, F. J., & Bachmann, O. (2013). On the longevity of large upper crustal silicic magma reservoirs. *Geology*, *41*(7), 759–762.
Gudmundsson, A. (1987). Formation and mechanics of magma reservoirs in iceland Geophysical Journal International, *91*(1), 27–41. https://doi.org/10.1111/j.1365-246x1987.tb05211.x
Gudmundsson, A. (2012). Magma chambers: Formation, local stresses, excess pressures, and compartments. *Journal of Volcanology and Geothermal Research*, *237-238*(Supplement C), 19–41. https://doi.org/10.1016/j.jvolgeores.2012.05.015
Gudmundsson, A. (2016). The mechanics of large volcanic eruptions. *Earth-Science Reviews*, *163*. https://doi.org/10.1016/j.earscirev.2016.10.003
Hildreth, W., & Lanphere, M. A. (1994). Potassium-argon geochronology of a basalt-andesite-dacite arc system: The Mount Adams volcanic field, Cascade Range of southern Washington. *GSA Bulletin*, *106*(11), 1413–1429. https://doi.org/10.1130/0016-7606(1994)106<1413:PAGOAB>2.3.CO;2
Huber, C., Bachmann, O., & Dufek, J. (2011). Thermo-mechanical reactivation of locked crystal mushes: Melting-induced internal fracturing and assimilation processes in magmas. *Earth and Planetary Science Letters*, *304*(3–4), 443–454. https://doi.org/10.1016/j.epsl.2011.02.022
Huber, C., Bachmann, O., & Manga, M. (2010). Two competing effects of volatiles on heat transfer in crystal-rich magmas: Thermal insulation vs defrosting. *Journal of Petrology*, *51*, 847–867.
Jellinek, A. M., & DePaolo, D. J. (2003). A model for the origin of large silicic magma chambers: Precursors of caldera-forming eruptions. *Bulletin of Volcanology*, *65*(5), 363–381. https://doi.org/10.1007/s00445-003-0277-y

Jerram, D. A., Cheadle, M. L., & Philpotts, A. R. (2003). Quantifying the building blocks of igneous rocks: Are clustered crystal frameworks the foundation? *Journal of Petrology*, *44*(11), 2033–2051. https://doi.org/10.1093/petrology/egg069

Karakas, O., Degruyter, W., Bachmann, O., & Dufek, J. (2017). Lifetime and size of shallow magma bodies controlled by crustal-scale magmatism. *Nature Geoscience*, *10*(6), 446–450. https://doi.org/10.1038/ngeo2959

Karlstrom, L., Dufek, J., & Manga, M. (2010). Magma chamber stability in arc and continental crust. *Journal of Volcanology and Geothermal Research*, *190*(3), 249–270. https://doi.org/10.1016/j.jvolgeores.2009.10.003

Landau, L. D., & Lifshitz, E. M. (1959). Theory of elasticity.

Le Mével, H., Gregg, P. M., & Feigl, K. L. (2016). Magma injection into a long-lived reservoir to explain geodetically measured uplift: Application to the 2007–2014 unrest episode at Laguna del Maule volcanic field, Chile. *Journal of Geophysical Research: Solid Earth*, *121*, 6092–6108. https://doi.org/10.1002/2016JB013066

Lejeune, A. M., & Richet, P. (1995). Rheology of crystal-bearing silicate melts: An experimental study at high viscosities. *Journal of Geophysical Research*, *100*(B3), 4215–4229. https://doi.org/10.1029/94JB02985

Lu, Z., & Dzurisin, D. (2010). Ground surface deformation patterns, magma supply, and magma storage at Okmok volcano, Alaska, from InSAR analysis: 2. Coeruptive deflation, July–August 2008. *Journal of Geophysical Research*, *115*, B00B03. https://doi.org/10.1029/2009JB006970

Marsh, B. D. (1989). Magma chambers. *Annual Review of Earth and Planetary Sciences*, *17*(1), 439–472. https://doi.org/10.1146/annurev.ea.17.050189.002255

Masterlark, T. (2007). Magma intrusion and deformation predictions: Sensitivities to the mogi assumptions. *Journal of Geophysical Research*, *112*, B06419. https://doi.org/10.1029/2006JB004860

Mastin, L. G., Roeloffs, E., Beeler, N. M., & Quick, J. E. (2008). Constraints on the size, overpressure, and volatile content of the Mount St. Helens magma system from geodetic and dome-growth measurements during the 2004–2006+ eruption. *U.S. Geological Survey Professional Paper*, *1750*, 461–488.

McTigue, D. F. (1987). Elastic stress and deformation near a finite spherical magma body: Resolution of the point source paradox. *Journal of Geophysical Research*, *92*(B12), 12,931–12,940. https://doi.org/10.1029/JB092iB12p12931

Mogi, K. (1958). Relations between the eruptions of various volcanoes and the deformations of the ground surfaces around them. *Bulletin of the Earthquake Research Institute*, *36*, 99–13.

Moitra, P., & Gonnermann, H. M. (2015). Effects of crystal shape- and size-modality on magma rheology. *Geochemistry, Geophysics, Geosystems*, *16*, 1–26. https://doi.org/10.1002/2014GC005554

Mourtada-Bonnefoi, C. C., Provost, A., & Albarède, F. (1999). Thermochemical dynamics of magma chambers: A simple model. *Journal of Geophysical Research*, *104*(B4), 7103–7115. https://doi.org/10.1029/1998JB900112

Nishimura, T. (2006). Ground deformation due to magma ascent with and without degassing. *Geophysical Research Letters*, *33*, L23309. https://doi.org/10.1029/2006GL028101

Nooner, S. L., & Chadwick, W. W. (2009). Volcanic inflation measured in the caldera of Axial Seamount: Implications for magma supply and future eruptions. *Geochemistry, Geophysics, Geosystems*, *10*, Q02002. https://doi.org/10.1029/2008GC002315

Parmigiani, A., Huber, C., & Bachmann, O. (2014). Mush microphysics and the reactivation of crystal-rich magma reservoirs. *Journal of Geophysical Research: Solid Earth*, *119*, 6308–6322. https://doi.org/10.1002/2014JB011124

Picard, D., Arbaret, L., Pichavant, M., Champallier, R., & Launeau, P. (2011). Rheology and microstructure of experimentally deformed plagioclase suspensions. *Geology*, *39*, 747–750. https://doi.org/10.1130/G32217.1

Pistone, M., Caricchi, L., Ulmer, P., Burlini, L., Ardia, P., Reusser, E., & Arbaret, L. (2012). Deformation experiments of bubble- and crystal-bearing magmas: Rheological and microstructural analysis. *Journal of Geophysical Research*, *117*, B05208. https://doi.org/10.1029/2011JB008986

Rice, J. R., & Cleary, M. P. (1976). Some basic stress diffusion solutions for fluid-saturated elastic porous media with compressible constituents. *Reviews of Geophysics*, *14*(2), 227–241. https://doi.org/10.1029/RG014i002p00227

Rivalta, E. (2010). Evidence that coupling to magma chambers controls the volume history and velocity of laterally propagating intrusions. *Journal of Geophysical Research*, *115*, B07203. https://doi.org/10.1029/2009JB006922

Segall, P. (2016). Repressurization following eruption from a magma chamber with a viscoelastic aureole. *Journal of Geophysical Research: Solid Earth*, *121*, 8501–8522. https://doi.org/10.1002/2016JB013597

Singer, B. S., Le Mével, H., Licciardi, J. M., Córdova, L., Tikoff, B., Garibaldi, N., & Feigl, K. L. (2018). Geomorphic expression of rapid Holocene silicic magma reservoir growth beneath Laguna del Maule, Chile. *Science Advances*, *4*(6), eaat1513. https://doi.org/10.1126/sciadv.aat1513

Singh, S., Anderson, J., & Rodríguez, M. (1998). Triggered seismicity in the Valley of Mexico from major Mexican earthquakes. *Geofísica Internacional*, *37*(1). Retrieved from http://www.redalyc.org/comocitar.oa?id=56837101

Sisson, T. W., & Bacon, C. R. (1999). Gas-driven filter pressing in magmas. *Geology*, *27*, 613–626. https://doi.org/10.1130/0091-7613(1999)027<0613:GDFPIM>2.3.CO;2

Sparks, R. S. J., & Cashman, K. V. (2017). Dynamic magma systems: Implications for forecasting volcanic activity. *Elements*, *13*(1), 35–40. https://doi.org/10.2113/gselements.13.1.35

Srigutomo, W., Trimadona, M. R., & Anwar, H. (2015). Modeling and inversion of volcanic surface deformation based on Mogi model and McTigue model. *AIP Conference Proceedings*, *1656*(1), 70016. https://doi.org/10.1063/1.4917162

Szymanowski, D., Wotzlaw, J. F., Ellis, B. S., Bachmann, O., Guillong, M., & von Quadt, A. (2017). Protracted near-solidus storage and pre-eruptive rejuvenation of large magma reservoirs. *Nature Geoscience*, *10*(10), 777–782. https://doi.org/10.1038/ngeo3020

Vigneresse, J. L., Barbey, P., & Cuney, M. (1996). Rheological transitions during partial melting and crystallization with application to felsic magma segregation and transfer. *Journal of Petrology*, *37*(6), 1579–1600. https://doi.org/10.1093/petrology/37.6.1579

Voight, B., Linde, A. T., Sacks, I. S., Mattioli, G. S., Sparks, R. S. J., Elsworth, D., & Williams, P. (2006). Unprecedented pressure increase in deep magma reservoir triggered by lava-dome collapse. *Geophysical Research Letters*, *33*, L03312. https://doi.org/10.1029/2005GL024870

Ward, K. M., Zandt, G., Beck, S. L., Christensen, D. H., & McFarlin, H. (2014). Seismic imaging of the magmatic underpinnings beneath the Altiplano-Puna volcanic complex from the joint inversion of surface wave dispersion and receiver functions. *Earth and Planetary Science Letters*, *404*, 43–53. https://doi.org/10.1016/j.epsl.2014.07.022

Wicks, CW., Dzurisin, D., Ingebritsen, S., Thatcher, W., Lu, Z., & Iverson, J. (2002). Magmatic activity beneath the quiescent Three Sisters volcanic center, central Oregon Cascade Range. *Geophysical Research Letters*, *29*(7), 1122. https://doi.org/10.1029/2001GL014205